Research Square

Preprints are preliminary reports that have not undergone peer review.
They should not be considered conclusive, used to inform clinical practice,
or referenced by the media as validated information.

Sealing performance of particle-adhered rough interfaces: Reconstruction of equivalent rough surfaces and contact-mechanics analysis

Haitao Zheng
Sanya Institute of Hunan University of Science and Technology
Jialiang Wang
Jialiangwang20190163.com

Sanya Institute of Hunan University of Science and Technology
Bo Li
Sanya Institute of Hunan University of Science and Technology
Lubo Tang
Sanya Institute of Hunan University of Science and Technology
Yongzheng Jang
Sanya Institute of Hunan University of Science and Technology
Buyan Wan
Sanya Institute of Hunan University of Science and Technology

Research Article

Keywords: particle contamination, rough-surface reconstruction, seal ring, pressure-retaining coring, sealing performance, contact mechanics

Posted Date: October 6th, 2026

DOI: https://doi.org/10.21203/rs.3.rs-11059977/v1

License: This work is licensed under a Creative Commons Attribution 4.0 International License.
Read Full License

Additional Declarations: No competing interests reported.

Sealing performance of particle-adhered rough interfaces: Reconstruction of equivalent rough surfaces and contact-mechanics analysis

Haitao Zheng[1 2 3], Jialiang Wang[* 1 2 3], Bo Li [1 2 3], Lubo Tang[1 3]Yongzheng Jang[1 3],Buyan Wan[1 2 3]

(1.Sanya Institute of Hunan University of Science and Technology, Sanya 572024, Hainan, China ; 2. National Local Joint Engineering Laboratory of Marine Mineral Resources Exploration Equipment and Safety Technology, Hunan University of Science and Technology, Xiangtan 411201, China; 3. School of Mechanical Engineering, Hunan University of Science and Technology, Xiangtan 411201, China)

Abstract: Solid-particle adhesion is an important factor contributing to the degradation of sealing interfaces, particularly in particle-laden operating environments such as subsea pressure-retaining coring, offshore oil and gas drilling and production, and pipeline transportation. In this study, an equivalent rough-surface reconstruction model incorporating particle adhesion and a three-dimensional finite-element method (FEM) contact model between the seal ring and the reconstructed particle-adhered surface are established. The effects of particle size and coverage on equivalent stress, contact pressure, real contact area, normal contact force, and sealing safety margin are investigated. The results show that the dominant asperities of the original rough surface primarily determine the locations of contact-pressure and equivalent-stress concentrations. Particle adhesion intensifies these local concentrations and results in a more nonuniform load distribution across the sealing interface. Particle size has a markedly greater influence on the interfacial contact state than particle coverage. For a particle size of 1.25 μm, the variations in both real contact area and normal contact force remain within 5%. When the particle size increases to 2.5 μm, the real contact area increases by approximately 9%, while the normal contact force increases by 8–14%. At 5 μm, both the normal contact force and average contact pressure increase by 15–25%. At a coverage of 10%, the safety-margin deviation generally remains below 0.03. For 2.5 μm particles, this deviation increases to approximately 0.09 with increasing coverage, whereas the 5 μm cases exhibit larger overall deviations. This study proposes a particle-adhered equivalent rough-surface reconstruction method that preserves the characteristics of the original rough surface and quantitatively

*Corresponding author .Tel.:+86-731-13507313232;

E-mail address:Jialiangwang2019@163.com

evaluates the effects of particle size and coverage on the sealing contact state, providing a methodological basis for performance evaluation and structural optimization of sealing interfaces operating in particle-laden environments.

Key words: particle contamination; rough-surface reconstruction; seal ring; pressure-retaining coring; sealing performance; contact mechanics

1. Introduction

With the ongoing transition of the global energy system and growing concerns over climate change, natural gas hydrates, owing to their enormous reserves, widespread occurrence, and clean combustion characteristics, are regarded as an important alternative clean energy resource (Kvenvolden, 1993; Ruppel & Waite, 2020). Because natural gas hydrates readily dissociate under ambient temperature and pressure, pressure-retaining coring is required for sample recovery. As shown in Fig. 1, compared with drilling vessels, seabed drilling rigs offer more pronounced advantages for detailed surveys involving dense borehole layouts in deep-water environments with water depths of several thousand metres and shallow formations with drilling depths of several hundred metres.

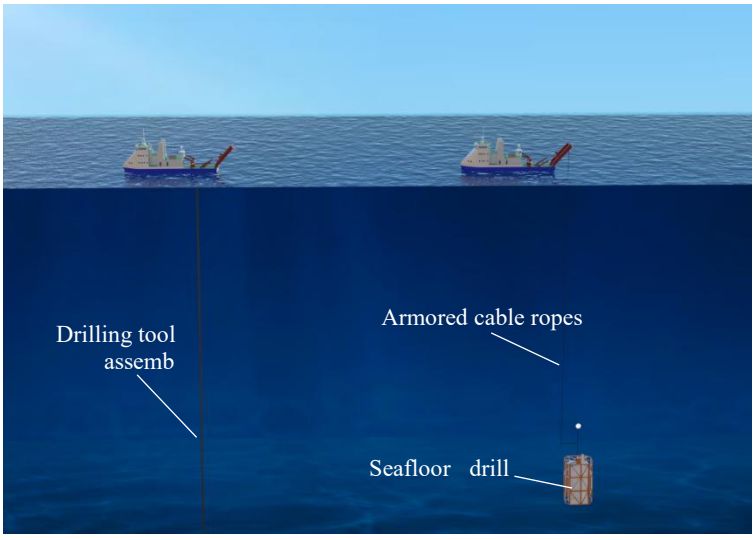


Fig.1 Seafloor exploration methods.

A key feature of pressure-retaining coring using seabed drilling rigs is that the core barrel itself serves directly as the pressure-retaining vessel. An automatically actuated check-valve assembly is installed at the upper end, whereas the lower end is sealed by a detachable

pressure-retaining cap. The sealing procedure of the pressure-retaining cap is illustrated in Fig. 2 (Wang et al., 2024). Before each drilling run, the threaded make-up and break-out device on the seabed drilling rig, assisted by a manipulator, separates the pressure-retaining cap from the drilling tool and temporarily stores it within the inner bore of the device, as shown in Fig. 2(a). After completion of the drilling run, the pressure-retaining cap is reattached to the lower end of the drilling tool using the same device with the assistance of the manipulator, thereby completing the sealing operation, as shown in Fig. 2(b). A Y-ring seal is installed in the seal gland of the pressure-retaining cap, with the outer surface of the core lifter case serving as its sealing surface. As illustrated in Fig. 3, two potential fluid leakage paths exist: (1) direct leakage along C.S.1 and (2) infiltration along C.S.3 followed by further penetration along C.S.2.

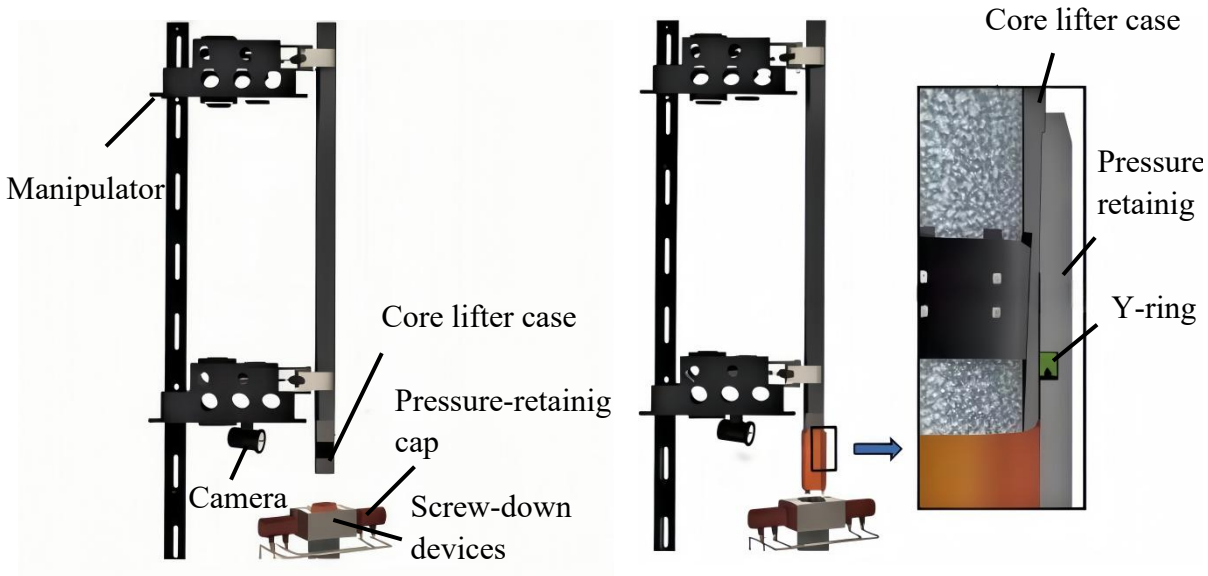


Fig.2 Working principle of pressure controller, (a) Before drilling process. (b) After drilling

During drilling in sedimentary formations, seawater inevitably contains a certain concentration of rock cuttings (Li et al., 2024; Wang et al., 2025). Although the cleaning system on the drilling rig can remove sediments adhering to the sealing surface of the core lifter case to some extent, rock cuttings suspended in the seawater trapped inside the pressure-retaining cap cannot be effectively removed. Once solid particles become trapped within the sealing interface, they may damage the sealing surface and disrupt the uniform transmission of interfacial pressure, thereby degrading the sealing performance and potentially leading to seal failure. Similar

particle-induced sealing problems are also encountered in engineering applications such as oil and gas drilling and production and pipeline transportation. Therefore, elucidating the effects of solid-particle adhesion on the contact state of rough sealing interfaces is of both theoretical significance and practical engineering relevance.

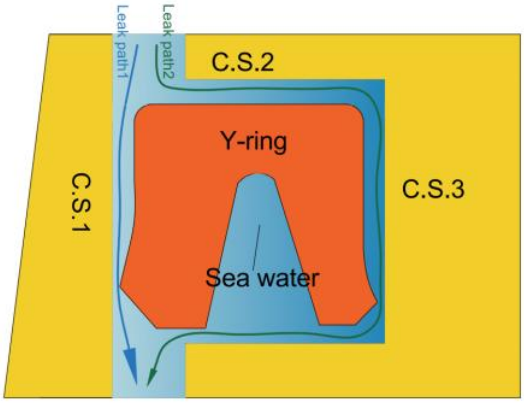


Fig.3 Leak path

In recent years, increasing attention has been devoted to the effects of solid-particle adhesion on the contact state of sealing interfaces. Zhou et al. (2021) investigated the wear process of sealing interfaces contaminated by SiO_2 particles and showed that particle adhesion aggravates local damage to the sealing surface. Qin et al. (2019) examined the effects of non-uniform particle sizes on the frictional characteristics of FKM O-ring seals and reported that particle contamination alters both the interfacial friction response and local load sharing. These findings indicate that the influence of particles on sealing interfaces extends beyond surface wear and is also closely associated with changes in the local contact state and load-transfer behaviour. When particles participate in interfacial contact, their size, morphology, and spatial distribution can all affect the mechanical response of the interface. Chern et al. (2022) employed the finite-element method to analyse the mechanical response of an O-ring in contact with solid particles and found that particle size affects the maximum contact stress in the initial contact region. Chitta et al. (2021) investigated the influence of particle morphology on contact behaviour from a contact-mechanics perspective and showed that particle adhesion can alter the local contact area and load distribution of sealing materials. Altuhafi et al. (2024) combined experiments and numerical simulations to examine deformation and load transfer during

solid-particle contact, demonstrating that particle size and shape influence the distributions of contact stress and local deformation. Li et al. (2023) employed multiscale experiments and modelling to investigate microscale damage within particle–contact regions and showed that factors such as particle morphology and hardness modify the local stress distribution. Xiao et al. (2024) used a coupled discrete-element method–finite-element method (DEM–FEM) approach to investigate multipoint contact between particle assemblies and compliant interfaces under high-pressure conditions, revealing that the spatial distribution and contact state of particles alter interfacial load-transfer paths and consequently affect local stress concentration. Collectively, these studies demonstrate that particle characteristics and their spatial distribution are important factors governing the contact response of sealing interfaces.

However, most existing studies simplify metallic sealing surfaces as smooth surfaces or regular geometries, making it difficult to capture the localised contact and non-uniform load transfer inherent to actual rough interfaces. Adhered particles interact with the original surface asperities and jointly modify the local topography and contact state. Therefore, an appropriate representation of the equivalent surface morphology after particle adhesion, while retaining the characteristics of the original rough surface, is essential for reliable analysis of sealing-interface contact behaviour. In addition, a comprehensive approach capable of jointly considering the real contact area, normal contact force, and average contact pressure to evaluate the overall deviation of the interfacial contact state remains lacking.

To address these issues, an equivalent rough-surface reconstruction method incorporating particle adhesion is developed in this study, and a three-dimensional finite-element method (FEM) contact model is employed to investigate the effects of particle size and coverage on the mechanical response of the sealing interface. The main contributions are as follows:

(1) An equivalent rough-surface reconstruction model incorporating particle-adhesion effects is established. By introducing a geometric correction term and a continuous smoothing procedure, local topographic variations caused by particle adhesion are represented while preserving the statistical characteristics of the original rough surface, thereby providing an equivalent surface model for subsequent sealing-contact analysis.

(2) A three-dimensional finite-element contact model between the seal ring and the equivalent rough metallic surface is developed. Particle size and coverage are taken as the primary variables to investigate their effects on contact-pressure distribution, von Mises stress, real contact area, and normal contact force, thereby characterising the evolution of the contact state of rough sealing interfaces under particle adhesion.

(3) A safety-margin evaluation method based on the sealing contact state is proposed. Using the particle-free condition as the reference, variations in real contact area, normal contact force, and average contact pressure under different particle sizes and coverages are compared to quantify the extent to which particle adhesion alters the sealing contact state.

The results provide a theoretical basis for the design and parameter optimisation of sealing systems operating in particle-laden environments encountered in marine exploration, oil and gas pipeline transportation, and related engineering applications.

2. Equivalent rough-surface reconstruction model with particle adhesion

Fig. 4 presents the overall methodological framework of this study. First, an equivalent rough surface is reconstructed from a numerically generated Gaussian rough morphology, and particle adhesion is introduced by superimposing discrete particle geometries onto the original height field. The reconstructed surfaces are then validated in terms of statistical characteristics, including the height distribution, autocorrelation function, and power spectral density. Subsequently, finite-element contact analysis is performed on the reconstructed sealing interface to obtain the normal contact force, real contact area, and average contact pressure, which are normalized against the particle-free reference condition. Finally, these contact-response indicators are incorporated into the safety-margin assessment to compare the sealing states under different particle condition

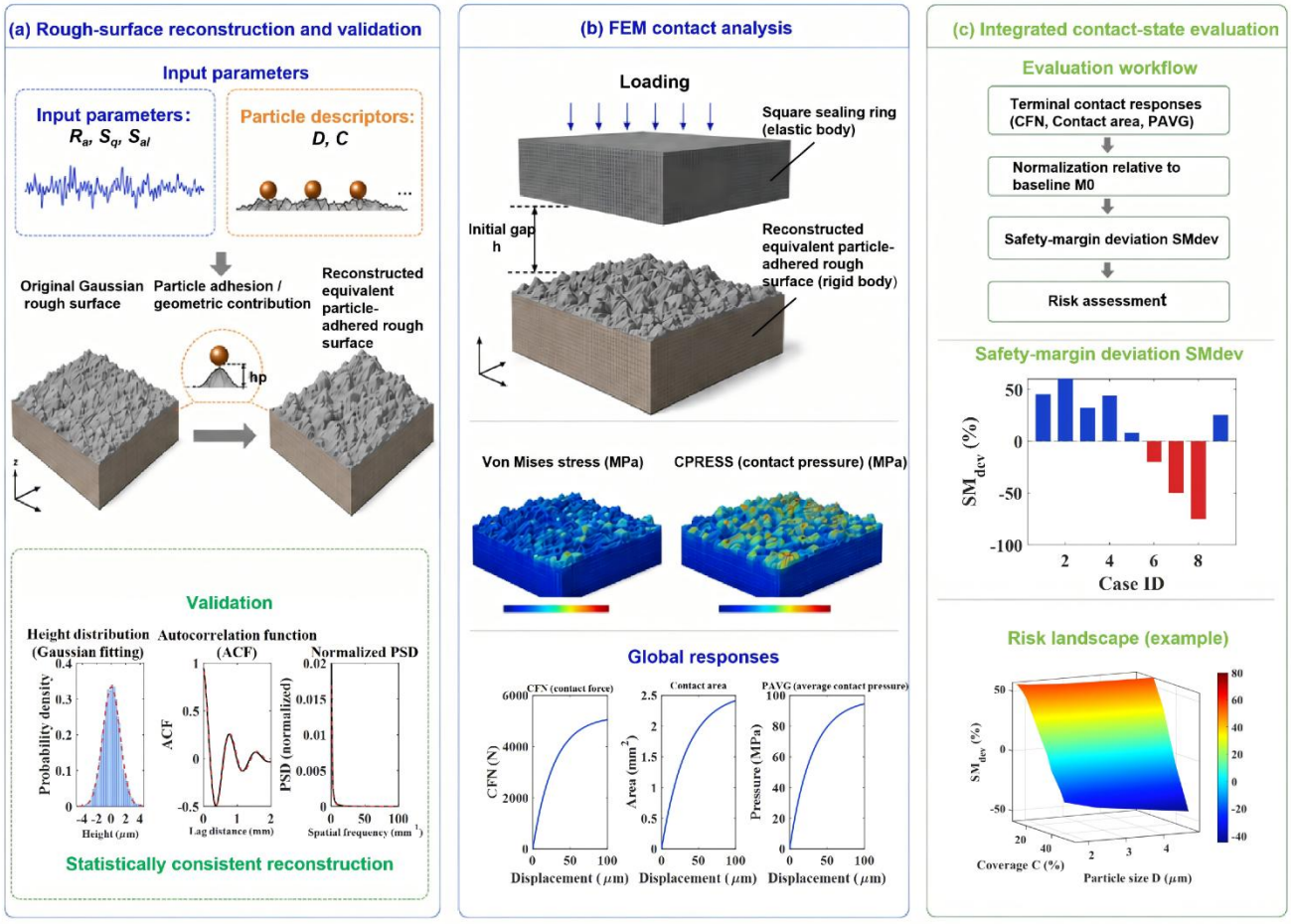


Fig.4. Overall methodological framework for rough-surface reconstruction

2.1 Numerical model for surface reconstruction

The sealing action at the seal ring–core lifter case interface essentially arises from intimate solid-to-solid contact between an elastic sealing material and a metallic substrate. Macroscopic conformity of the sealing pair depends on microscale mechanical interlocking between the rough surfaces. Therefore, the microstructural characteristics of the contact interface play an important role in the overall sealing performance. Fig. 5 illustrates the microtopography of the contact interface on the core lifter case.

Rough-surface contact models are widely used to investigate the interfacial behaviour of sealing pairs. Three-dimensional rough surfaces are generally reconstructed using statistical principles and mathematical topography models to reproduce the statistical characteristics of actual contact interfaces. A rough surface can be characterised by two principal features. The first is the **height distribution**, which describes the statistical distribution of surface elevations and reflects the asperity peaks, valleys, and overall amplitude of surface undulations. The second is the **spatial distribution**, which describes the correlation and continuity of surface heights in

the spatial domain. The former primarily characterises surface-amplitude information, whereas the latter describes spatial correlation and topographic structure (Jia-Nan Li et al., 2021). The roughness parameters used to characterise the surface morphology are listed in Tab. 1.

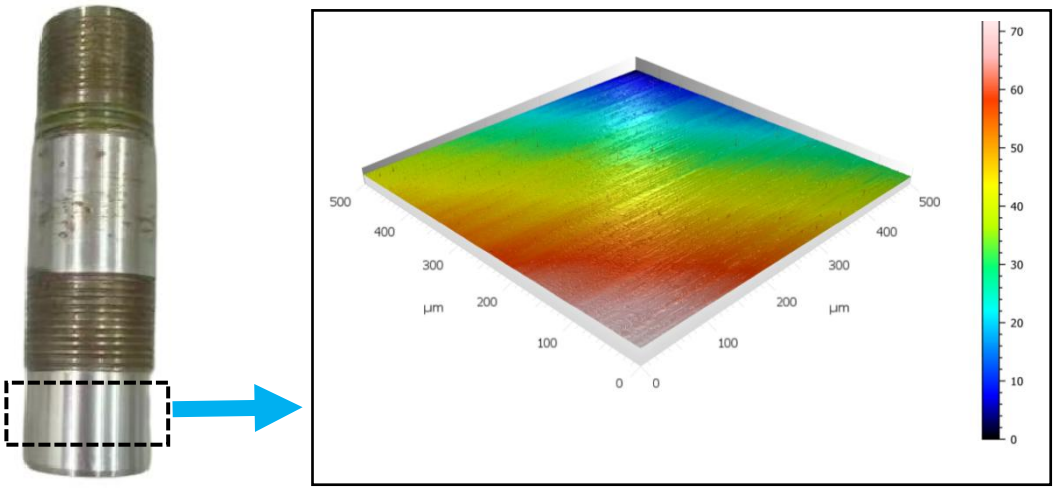


Fig.5 Micro-contact morphology at the sealing interface

Tab.1 Surface roughness characterisation

ParameterType	Parameter Name and Symbo
AmplitudeParameters	Root-mean-square height **Sq**; Arithmetic mean deviation **Sa**; Maximum height **Sz**; Skewness **Sk**; Kurtosis **Ku**
Spatial Parameters	Autocorrelation length **Sal**

Let the original surface height field be $z_0(x,y)$ as a function of x and y. Its characteristic parameters include the root-mean-square height S_q, the arithmetic mean deviation S_a, the skewness S_{sk}, the kurtosis Ku, and the autocorrelation length S_{at}. Their mathematical definitions are given as follows.

The amplitude parameters of a rough surface primarily reflect the height-distribution characteristics and are key descriptors of the micro-topography of a sealing surface. The root-mean-square height S_q represents the root-mean-square value of the height distribution over the sampled area, and is expressed as:

$$S_q = \sqrt{\frac{1}{A}\iint_A z^2\,(x,y)\,dx\,dy} \tag{1}$$

The arithmetic mean deviation S_a is the arithmetic mean of the absolute surface heights within the sampled area.

$$S_a = \frac{1}{A}\iint_A |z(x,y)|\;dx\,dy \tag{2}$$

The skewness Sk describes the symmetry of the surface-height probability distribution within the sampled area, and its magnitude reflects the degree of deviation from the mean height. When Sk=0, the height distribution is symmetric and exhibits Gaussian characteristics. When Sk<0, the distribution is left-skewed and the rough surface is characterised by sharper valleys. When Sk>0, the distribution is right-skewed and the rough surface is characterised by sharper peaks.

$$Sk = \frac{1}{S_q^3}\left[\frac{1}{A}\iint_A z^3\,(x,y)\,dx\,dy\right] \tag{3}$$

The kurtosis Ku characterises the sharpness of the surface-height probability distribution within the sampled area. When Ku=3, the height distribution is Gaussian. A larger Ku indicates more extreme height values, meaning that the surface contains more pronounced high peaks and deep valleys. A smaller Ku indicates fewer extremes, corresponding to a surface with fewer high peaks and deep valleys, as defined in (ISO, 2012).

$$Ku = \frac{1}{S_q^4}\left[\frac{1}{A}\iint_A z^4\,(x,y)\,dx\,dy\right] \tag{4}$$

The height distribution of points on a rough surface is not completely independent. The dependency between surface heights at different spatial locations is characterised by the autocorrelation function (ACF). The mathematical expression of the autocorrelation function is given as (Lehmann et al., 1997):

$$R_z(k,l) = E\{z(I,J)z(I+k,J+l)\} \tag{5}$$

where z(I,J) denotes the height distribution sequence of the rough surface, which is treated as a discrete stationary random process.Under the ergodic assumption, the autocorrelation function can be expressed as:

$$R_z(k,l)=\frac{1}{MN}\sum_{I=0}^{N-1}\sum_{J=0}^{M-1} z(I,J)z(I+k,J+l) \tag{6}$$

M and N denote the numbers of sampling points of the rough surface in the x and y directions, respectively. The spatial parameters are derived from the autocorrelation function and characterise the lateral distribution features of the rough surface.

The autocorrelation length S_{at} is defined as the horizontal distance at which the autocorrelation function first decays to a specified value s , typically taken as 0.1(ISO, 2012).The expression is given as follows:

$$S_{at}=\min_{\tau_x,\tau_y\in R}\left(\sqrt{\tau_x^2+\tau_y^2}\right), R=\left\{(\tau_x,\tau_y): f_{ACF}(\tau_x,\tau_y)\le s\right\} \tag{7}$$

Here, τ_x and τ_y denote the autocorrelation lengths in the x and y directions, respectively. The generation of a rough surface is a stochastic process, and each realization of the surface is entirely different. Since surface roughness represents an average statistical concept, rough surfaces with identical height parameters can be regarded as equivalent.

Previous studies have shown that the equivalent rough peak height distribution after accounting for adhered solid particles is consistent with a Gaussian height distribution. Therefore, in the subsequent modelling and analysis, a Gaussian distribution is adopted to characterise the height features(Goryacheva et al., 2024). Its probability density function is given as follows:

$$p(z)=\frac{1}{\sqrt{2\pi}\sigma}\exp\left[-\frac{(z-\mu)^2}{2\sigma^2}\right] \tag{8}$$

In general, the autocorrelation function of engineering rough surfaces can be well approximated by an exponential form. Therefore, in this study, an exponential autocorrelation function is adopted to construct the equivalent rough peak surface of the circlip groove seat. The expression of the exponential autocorrelation function is given as follows:

$$R(k,l)=S_q^2\exp\left\{-2.3\left[\left(\frac{k}{\tau_x}\right)^2+\left(\frac{l}{\tau_y}\right)^2\right]\right\} \tag{9}$$

τx and τy denote the autocorrelation lengths in the x and y directions, respectively. When the autocorrelation lengths differ, the spatial distribution characteristics of the rough surface also differ, thereby determining the surface texture direction. If τx=τy, the surface is isotropic; if τx≠τy, the surface is anisotropic. Here, k and l represent the sampling points in the x and y directions, respectively.

In the above expression, S_q is the standard deviation of the surface height, also referred to as the root-mean-square roughness. In engineering practice, surface roughness is often characterised by the arithmetic mean deviation Ra (i.e., Ra=Sa). There exists a certain correspondence between S_q and Ra; specifically, their relationship with the standard deviation can be expressed as (Zhao et al., 2006):

$$S_q=1.25R_a \tag{10}$$

When solid particles adhere to the surface, the above parameters alone cannot adequately reflect the micro-scale morphological changes. Therefore, geometric correction characteristics and continuity correction characteristics are further introduced.

Based on the local protrusion effect induced by particle adhesion, the geometric correction characteristic incorporates the geometric parameters of a single particle $\left(h_i,r_i,\rho_p\right)$, which represent the particle height, radius, and distribution density, respectively, to characterise their influence on the microscopic surface topography. The continuity correction characteristic is implemented through the smoothing operator S_σ, which performs interpolation and convolution on the modified surface morphology to achieve spatial continuity of the rough surface.

Before establishing the particle-adhered rough-surface reconstruction model, the particle-generation process and its relationship with the surface-height field are first defined, as illustrated in Fig. 6. Fig. 6(a) presents the engineering configuration of the rough sealing interface with adhered particles. An initial clearance exists between the square-section seal ring

and the metallic substrate, while the original rough surface provides the geometric substrate for particle adhesion. An initial height field is generated according to the prescribed roughness and associated statistical parameters, after which particles with controlled size and coverage are randomly distributed over the surface.

Because the effect of particle adhesion depends on the local peak–valley morphology of the original surface, particles located at different topographic positions produce different local height increments. Particle adhesion therefore does not simply shift the mean surface height. Instead, it modifies the local height distribution through the geometric contribution of individual particles. Based on the geometry of each particle, the corresponding local height contributions are superimposed on the original height field to obtain the initial particle-adhered reconstructed surface:

$$z_g(x,y) = z_0(x,y) + \sum_{i=1}^{N_p} \Delta z_i(x,y) \quad (11)$$

As shown in Fig. 6(b), the particle-adhered height field is subsequently subjected to a continuity treatment to eliminate local geometric discontinuities resulting from the direct superposition of discrete particles:

$$z_s(x,y) = G_\sigma(x,y) \times z_g(x,y) \quad (12)$$

A roughness-normalisation correction is then applied so that the final equivalent rough surface $z_{eq}(x,y)$ retains the topographic characteristics induced by particle adhesion while maintaining the prescribed statistical roughness parameters.

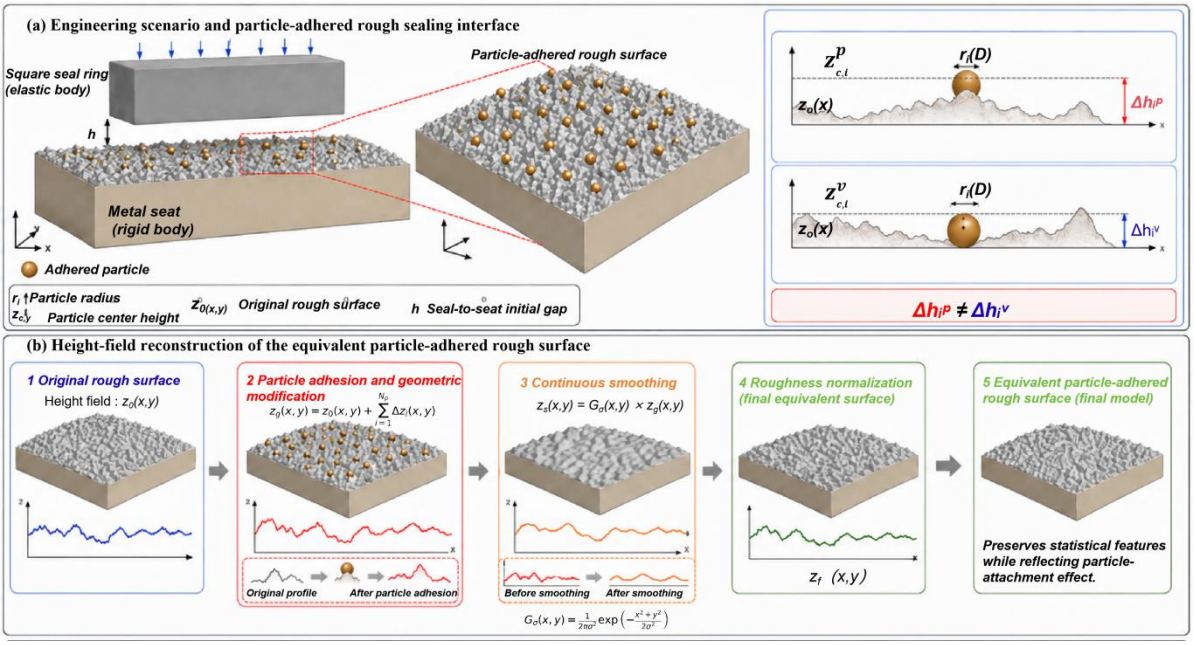


Fig.6 Schematic of the particle-attachment-based reconstruction of a rough sealing interface. (a) Engineering configuration and local particle-attachment mechanisms.(b) Height-field reconstruction from the original rough surface to the equivalent particle-adhered rough surface.

It should be noted that the particle height shown in the figure is only a schematic representation of the geometric profile. In the actual calculation, the local height function of a single particle, $z_{p,i}(x,y)$, is continuously described according to Eqs. (13)–(21). The adhered height field is then normalized through geometric correction parameters and continuity correction parameters to prevent the overall roughness from deviating beyond the designed range due to particle adhesion.

When spherical particles with a diameter D and surface coverage C adhere to the surface, they induce local geometric modifications to the original surface morphology. For modelling convenience, the particles are assumed to be randomly and uniformly distributed over the surface, and the particle center heights satisfy the prescribed geometric constraints:

$$z_p(x,y)=\begin{cases}\sqrt{r_p^2-(x-x_i)^2-(y-y_i)^2}-(r_p-h_0), & (x,y)\in\Omega_i\\ 0, & \text{elsewhere}\end{cases} \tag{13}$$

Here, $r_p=D/2$; (x_i,y_i) denotes the center coordinates of the i -th particle; Ω_i represents the projection region of the particle on the surface; and h_0 is the equivalent elevation height after the particle comes into contact with the substrate.

When a particle is located at two typical positions—namely, on a surface asperity peak or within a valley—the corresponding equivalent geometric correction terms are given as follows:

$$h_{01}=h+D, \quad h_{02}=h+\sqrt{r_p^2-\frac{D^2}{4}}+r_p\tan(\theta_0/2) \tag{14}$$

In the above expressions, h denotes the original surface height, and θ_0 represents the initial surface micro-slope angle.

The equivalent surface height field after particle adhesion can be expressed as:

$$z'(x,y)=z_0(x,y)+\sum_{i=1}^{N_p} z_p(x-x_i,y-y_i) \tag{15}$$

where $N_p=C\frac{A}{\pi D^2}$ is the number of particles per unit area.

The geometric correction component of the model reflects the local modification of the surface height caused by particles adhering at different positions (asperity peaks or valleys).

To avoid abrupt height variations induced by particle adhesion and to ensure physical continuity and smoothness of the surface, a smoothing operator S_σ is introduced. The geometrically corrected surface is spatially smoothed as follows:

$$z_s(x,y)=S_\sigma[z'(x,y)]=\iint z'(x,\xi)G_\sigma(x-\xi,y-\eta)\,d\xi\,dC \tag{16}$$

where $G_\sigma(x,y)$ is the two-dimensional Gaussian kernel function,

$$G_\sigma(x,y)=\frac{1}{2\pi\sigma^2}\exp\left[-\frac{x^2+y^2}{2\sigma^2}\right] \tag{17}$$

Here, σ is the smoothing scale, with a typical range of $0.3d_p\le\sigma\le0.6d_p$.

After geometric correction and continuity treatment, the final equivalent rough surface morphology model can be expressed as:

$$z_f(x,y)=\frac{S_q^*}{S_q'}S_\sigma\left[z_0(x,y)+\sum_{i=1}^{D}z_p\left(x-x_i,y-y_i\right)\right] \quad (18)$$

The root-mean-square roughness of the smoothed surface is given by:

$$S_q'=\sqrt{\frac{1}{A}\iint_A[z_s(x,y)-z_s]^2\ dxdy} \quad (19)$$

where $z_0(x,y)$ is the original surface, $z_p(x,y)$ represents the geometric contribution of particles, and S_σ is the continuity smoothing operator, reflecting the compliant response and local diffusion effect during particle adhesion. S_q^* denotes the target root-mean-square roughness.

For the smoothed surface, the autocorrelation function (ACF) is modified as:

$$R_s(\tau_x,\tau_y)=\frac{1}{A}\iint_A z_f(x,y)z_f(x+\tau_x,y+\tau_y)\,dxdy, \quad (20)$$

The corresponding correlation length l_c can be determined from the distance at which $R_s(\tau_x,\tau_y)=0.1$.

$$l_c=\min\{\sqrt{\tau_x^2+\tau_y^2}/R_s(\tau_x,\tau_y)\le 0.1\}. \quad (21)$$

2.2 Model validation

To evaluate the feasibility of the proposed equivalent reconstruction method for particle-adhered rough surfaces, the target roughness and height-distribution characteristics of the generated surfaces are first examined. The equivalent particle-adhered surfaces are then compared with explicitly reconstructed particle-adhered reference surfaces in terms of spatial correlation and spectral characteristics.

2.2.1Statistical validation of the numerical rough surfaces

To determine whether the generated numerical rough surfaces satisfy the prescribed statistical requirements, their roughness parameters and height distributions are analysed. Target

arithmetic mean roughness values of Ra=0.8, 1.6, and 3.2 μm are considered. For each roughness level, an original rough surface and a corresponding equivalent particle-adhered surface are generated, giving a total of six numerical surfaces. Each surface has dimensions of 200 μm × 200 μm and is discretised into a 200 × 200 grid containing 40,401 nodes. The resulting morphologies at different target roughness levels are shown in Fig. 7.。

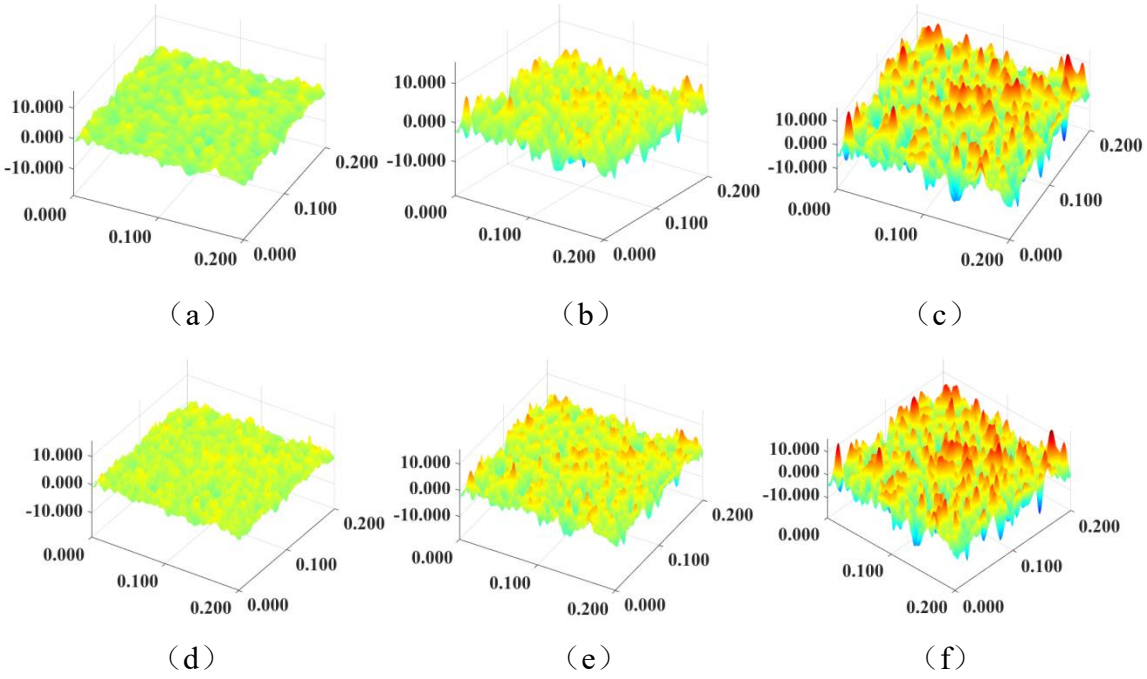


Figure.7 Surface topography of the six constructed rough surfaces；(a–c) Raw surfaces with arithmetic mean roughness values Ra = 0.8μm,1.6μm, and 3.2μm, respectively.(d–f).Corresponding particle-attached surfaces reconstructed under the same baseline roughness levels

The nodal heights are demeaned before their probability distributions are evaluated, as shown in Fig. 8. As the target Ra increases from 0.8 to 3.2 μm, the range of the height distribution progressively broadens, indicating a corresponding increase in the amplitude of surface undulations. For both the original and particle-adhered surfaces, the height distributions remain concentrated around the mean and are approximately symmetric, consistent with the fundamental characteristics of a Gaussian random surface.

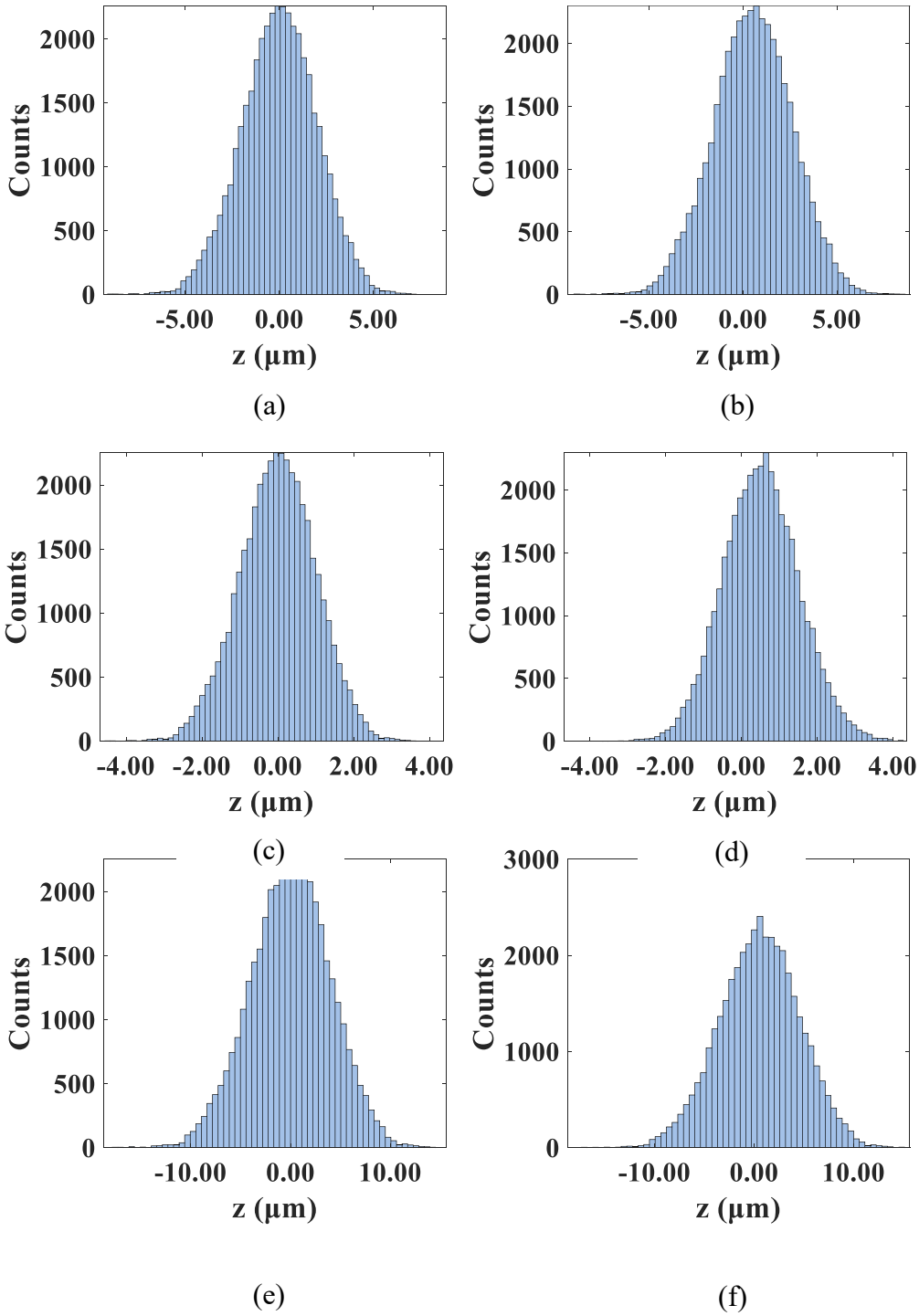


Fig.8 Height distribution histograms of six rough surfaces with different arithmetic mean heights;Height distribution histograms of the original surfaces (a,c,e). and the particle-attached surfaces (b, d, f). at three roughness levels (Ra = 0.8 μm, 1.6 μ m, and 3.2 μm)

Fig. 9 further compares the height probability density distributions of the original and particle-adhered surfaces together with their Gaussian fits. All distributions agree well with the

corresponding Gaussian curves, indicating that particle adhesion does not alter the basic form of the height distribution. Following particle adhesion, the probability-density peak increases and the distribution becomes narrower, indicating that a larger proportion of nodal heights is concentrated around the mean. The difference between the original and particle-adhered surfaces gradually diminishes as the target roughness increases.

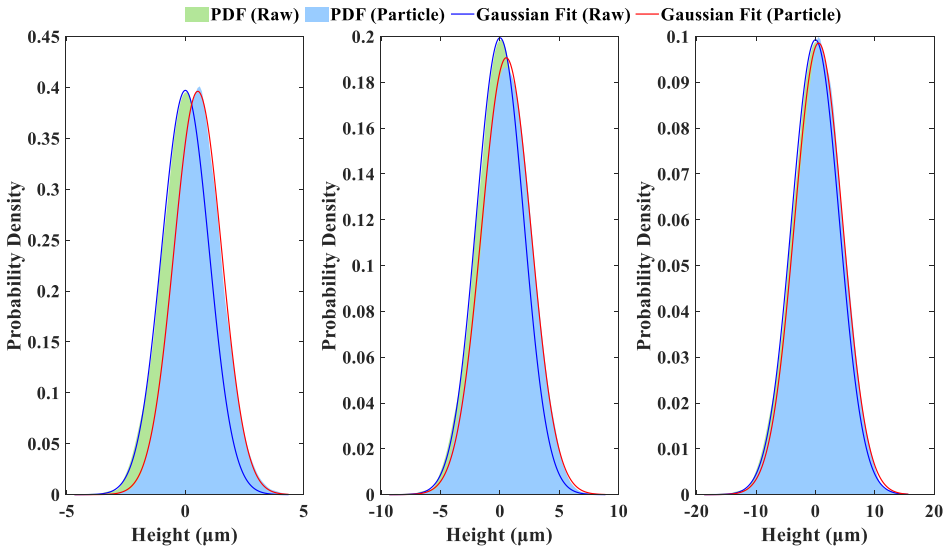


Fig.9 Comparison of height distribution between the originaland particle-attached surfaces at three roughness levels.(a)Ra=0.8.(b)Ra=1.6.(c)Ra=3.2

The statistical parameters of the six surfaces are listed in Tab. 2. The calculated Ra_0 values agree closely with their prescribed target values, demonstrating that the proposed method provides effective control over the overall roughness level of the generated surfaces. Only minor variations in Ra_0 and Sq_0 occur before and after particle adhesion, indicating that the equivalent reconstruction primarily modifies the local morphology without substantially changing the overall amplitude of surface roughness. The skewness Ssk ranges from −0.115 to −0.073, whereas the kurtosis Sku ranges from 3.037 to 3.109. These values indicate that the generated height distributions remain approximately symmetric, with kurtosis values close to the theoretical Gaussian value of 3.

Tab.2 Statistical parameters of six rough surfaces

Target Ra(μm)	Surface type	Ra_0 (μm)	Sq_0 (μm)	Ssk	Sku
0.8	Original	0.8036	1.0045	-0.11101	3.0896
0.8	Particle-attached	0.8055	1.0069	-0.07683	3.1087
1.6	Original	1.6000	2.0000	-0.11101	3.0896
1.6	Particle-attached	1.6732	2.0915	-0.07317	3.0369
3.2	Original	3.2145	4.0181	-0.11101	3.0896
3.2	Particle-attached	3.2328	4.0471	-0.11490	3.0817

Overall, the proposed rough-surface generation method reproduces the prescribed roughness levels while retaining the Gaussian characteristics of the height distribution. The equivalent particle-adhesion reconstruction introduces local topographic modifications without appreciably altering the overall roughness level or the basic form of the height distribution. These results validate the capability of the method to control the global statistical characteristics of the reconstructed surfaces.

2.2.2Morphological validation of the equivalent particle-adhered rough surfaces

To further evaluate the ability of the proposed equivalent reconstruction method to represent particle-adhered surface morphology, an explicit particle-adhered reference model is constructed, as shown in Fig. 10. In this reference model, discrete particles are generated directly on the original rough surface, thereby retaining their spatial distribution more explicitly. Because the particle size, coverage, and adhesion locations of micrometre-scale particles are difficult to control simultaneously in experiments, a computationally generated reference model is adopted to provide controllable particle-adhesion conditions.

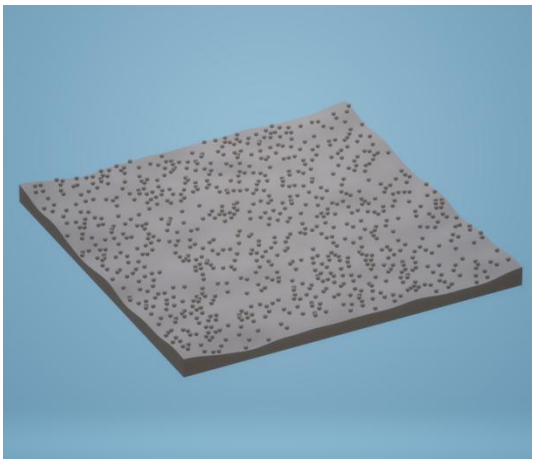


Fig.10Schematic diagram of the realistic adhesion model

The reference model uses a Gaussian rough surface as the original substrate. The particle diameter is fixed at the prescribed value, with the corresponding radius, and particle coverages of 10%, 30%, and 50% are considered. Particle positions in the surface plane are generated randomly, subject to a non-overlap constraint. For the i th particle at a prescribed planar location(x_i,y_i), the particle is assumed to settle vertically from above until it first contacts the original rough surface. Its centre height is determined by:

$$z_{c,i}=\max_{r_i\le R}\left[z_0(x,y)+\sqrt{R^2-r_i^2}\right]-\delta \tag{22}$$

Where ，

$$r_i=\sqrt{(x-x_i)^2+(y-y_i)^2} \tag{23}$$

r_i denotes the lateral distance from a surface point to the projected center of the ith particle, and δ is a small embedment depth introduced to account for the local adhesion between the particle and the rough surface.

Surface morphology cannot be adequately characterized by a single roughness parameter alone. Its spatial correlation and spectral characteristics must also be considered (Pérez-Ràfols and Almqvist, 2019; Wang et al., 2021; Rodriguez et al., 2025). Therefore, the autocorrelation function (ACF) is employed to characterize the variation in surface-height correlation with lateral distance, while the normalized power spectral density (PSD) is used to compare the relative distribution of roughness components over different spatial scales.

Fig. 11 compares the ACFs and corresponding Gaussian fits of the equivalent particle-adhered surfaces and the explicit particle-adhered reference surfaces under different particle coverages. For both surface representations, the ACF gradually decays toward zero with increasing lateral distance ***r***, indicating a progressive weakening of the spatial correlation between surface heights. Under the M_2, M_5, and M_8 conditions, the two types of surfaces exhibit similar overall ACF trends and comparable characteristic distances over which the height correlation diminishes. These results indicate that the equivalent reconstruction preserves the principal spatial-correlation characteristics of the particle-adhered rough surface.

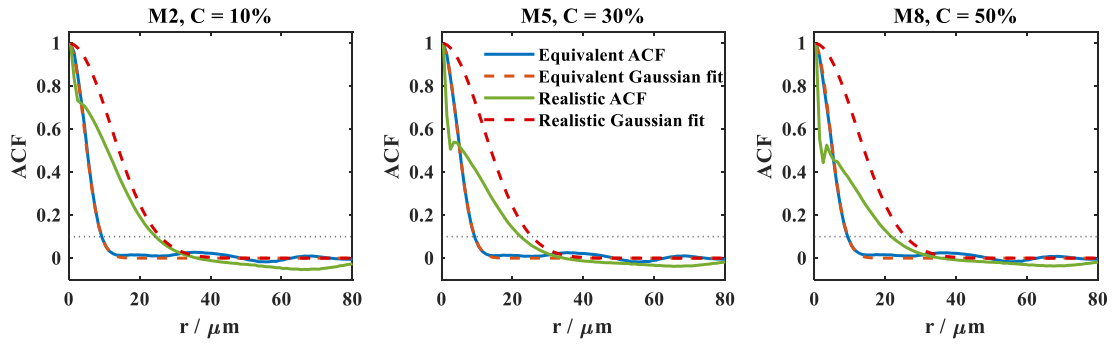


Fig.11 Autocorrelation-function comparison and Gaussian fitting

Fig. 12 compares the normalized PSDs of the equivalent particle-adhered surfaces and the explicit particle-adhered reference surfaces. For both surface representations, the normalized

PSD generally decreases with increasing spatial frequency q, indicating that the surface morphology is dominated by roughness components at relatively large spatial scales, whereas the contribution of small-scale features progressively decreases. At particle coverages of 10%, 30%, and 50%, the two surface representations exhibit similar overall spectral distributions, demonstrating that the equivalent reconstruction retains the principal distribution characteristics of surface roughness across different spatial scales.

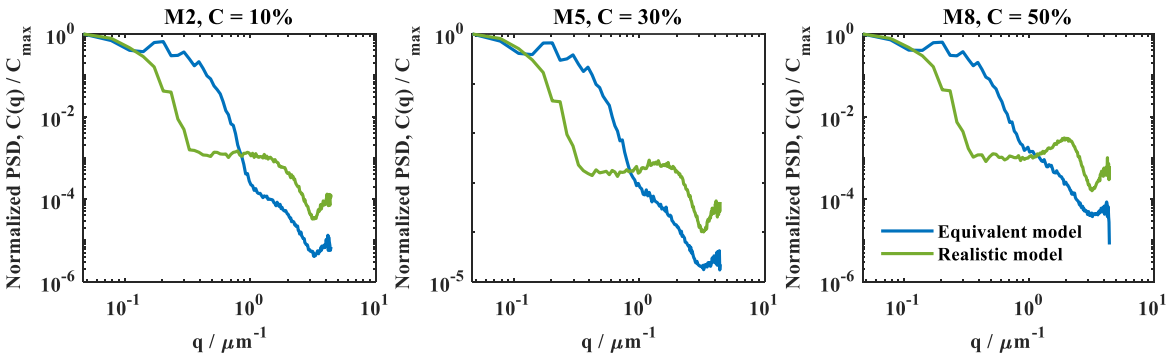


Fig.12 Normalized power spectral density comparison

The local differences between the two surface representations mainly arise from their different construction approaches. The explicit particle-adhered reference surface retains the geometrical contours and boundaries of individual particles, as well as the randomness of interparticle spacing, and therefore exhibits more pronounced local fluctuations over short-to-intermediate correlation distances and within parts of the medium-to-high spatial-frequency range. In contrast, the equivalent particle-adhered surface becomes relatively smoother after geometric correction and continuity treatment. Nevertheless, the two representations remain consistent in terms of their overall autocorrelation behavior, characteristic correlation-distance range, and dominant spectral distribution. These results demonstrate that the proposed equivalent reconstruction method can effectively reproduce the principal morphological characteristics of particle-adhered rough surfaces.

3. Contact Model

Particle adhesion is modelled on the original rough surface with Ra=0.8μm by combining three particle coverages, C=10%, 30%, and 50%, with three particle sizes, D=1.25, 2.5, and 5 μm. Together with the particle-free original rough surface at Ra=0.8μm as the reference case, ten

Gaussian rough-surface models with different particle-adhesion characteristics are established. For clarity in the subsequent analysis, the ten models are designated as listed in Tab. 3.

Tab.3 Naming of Different Models

(C%,Dμm)	Origin plane	(10,1.25)	(10,2.5)	(10,5)	(30,1.25)
Model	M_0	M_1	M_2	M_3	M_4

(C%,Dμm)	(30,2.5)	(30,5)	(50,1.25)	(50,2.5)	(50,5)
Model	M_5	M_6	M_7	M_8	M_9

The particle-adhered rough surfaces are discretised using the same meshing strategy described above. The seal ring is discretised through adaptive remeshing, resulting in approximately 16,000 elements, with the element type set to C3D8R. Fig. 13 illustrates the displacement-controlled loading scheme adopted for the local rough-surface contact model. The lower boundary of the model is defined as a reference plane, which remains fixed throughout the simulation. The load plane represents the final position of the seal ring after downward compression. The lower surface of the seal ring is simplified as an initial rigid plane located at a distance H0 from the reference plane, where H_0 represents the initial clearance of the local contact region. Mechanical loading is imposed by prescribing a downward displacement ΔX of the rigid plane along the negative y-direction. In the present model, H_0=50μm and ΔX=10μm. The loading step lasts 1 s. Normal contact is defined using the “hard” contact formulation, while the tangential behaviour is assumed to be frictionless. Geometric nonlinearity is accounted for by activating the “Nlgeom” option.

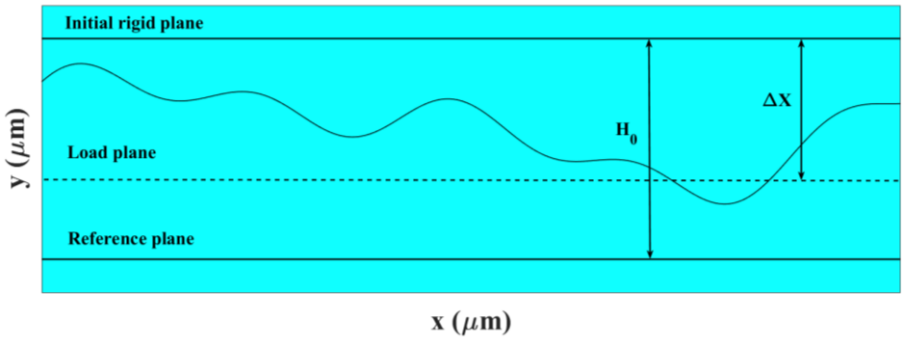


Fig.13 Displacement Loading Diagram

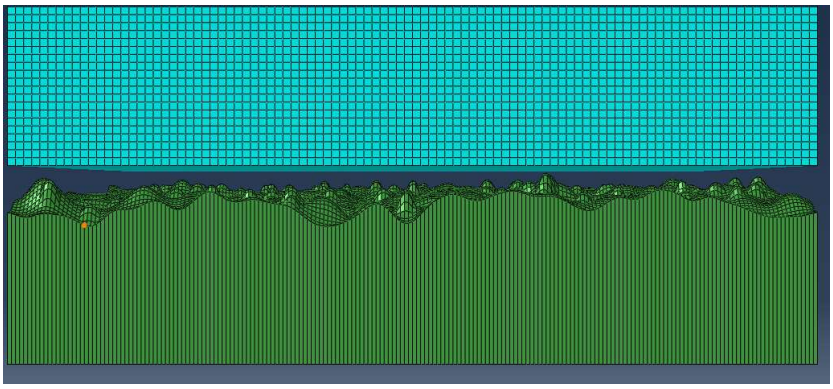


Fig.14 Pre-contact model of sealing systems in abaqus

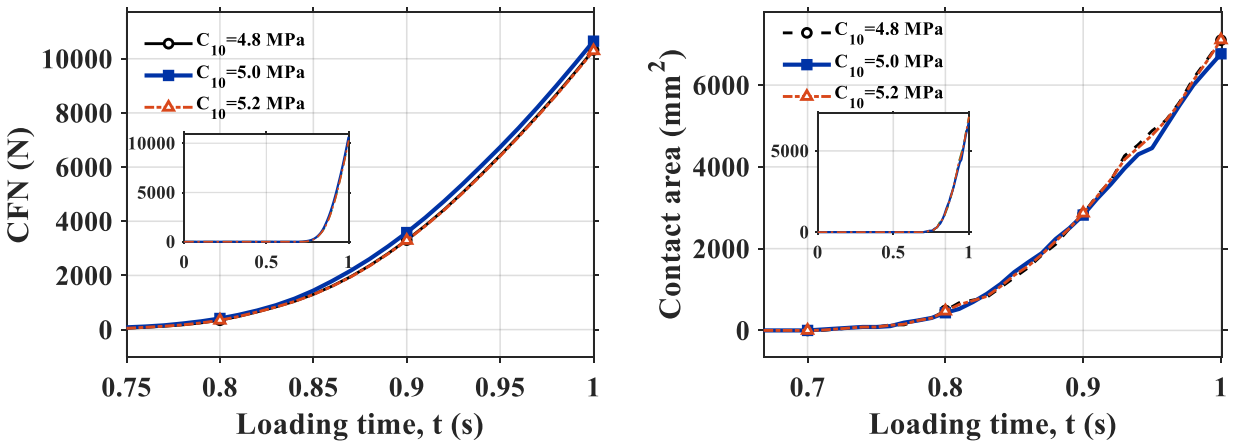
Fig. 14 shows the three-dimensional pre-contact model of the sealing system established in ABAQUS. Although the material properties of the adhered particles differ from those of the metallic substrate, both are substantially stiffer than the polyurethane seal ring. Accordingly, the material mismatch between the particles and the metallic substrate is expected to have only a limited influence on the overall contact-response trends considered here. The particle-adhered rough surface is therefore represented in the numerical model as an equivalent metallic body with homogeneous material properties. Q235 steel is assigned to the equivalent rough surface, with an elastic modulus of E=210GPa and a Poisson's ratio of ν=0.3.The seal ring is modelled as a polyurethane elastomer, and its large-deformation behaviour is described using a two-parameter Mooney–Rivlin model. The material is assumed to be isotropic and nearly incompressible, while viscoelasticity and material damage are neglected. The strain-energy density function is expressed as：

$$U=c_{10}\left(\bar{I}_1-3\right)+c_{01}\left(\bar{I}_2-3\right)+\frac{1}{D_1}\left(F^d-1\right)^2 \tag{24}$$

where U is the strain energy density, $\bar{I}1$ and $\bar{I}2$ are the first and second invariants of the deviatoric strain tensor, respectively, D1 is the volumetric compressibility parameter, and Jel is the elastic volume ratio. The seal ring in this study is made of polyurethane with a hardness range of 90–95A. Considering the relatively high finite-strain modulus of this type of material, a representative initial shear modulus of G_0=11 MPa is adopted (Seal Maker, 2021). For the two-parameter Mooney–Rivlin model, the initial shear modulus satisfies $G_0=2(C_{10}+C_{01})$ (Duncan et al., 2000; Kut and Ryzińska, 2023). A value of C_{10}=4.96 MPa has been reported in a previous

polyurethane contact analysis. Accordingly, C_{10}=5 MPa is adopted in this study (Lee et al., 2011), and C_{01}=0.5 MPa is obtained from $G_0=2(C_{10}+C_{01})$ while satisfying the target initial shear modulus.

To further examine the influence of the Mooney–Rivlin parameter values on the contact response, a material-parameter sensitivity analysis is conducted. With the initial shear modulus maintained at G_0=11 MPa, three values of C_{10}, namely 4.8, 5.0, and 5.2 MPa, are compared, with the corresponding C_{01} values adjusted to 0.7, 0.5, and 0.3 MPa, respectively, to satisfy $G_0=2(C_{10}+C_{01})$. The geometry, mesh, boundary conditions, and contact settings are kept identical for all models. As shown in Fig. 15, the variations in CFN and contact area among the different parameter sets are approximately 5%, indicating that, under the same initial stiffness, small variations in C_{10} around 5 MPa have a limited influence on the overall contact state. Therefore, the use of C_{10}=5 MPa and C_{01}=0.5 MPa as the baseline material parameters is considered reasonable.

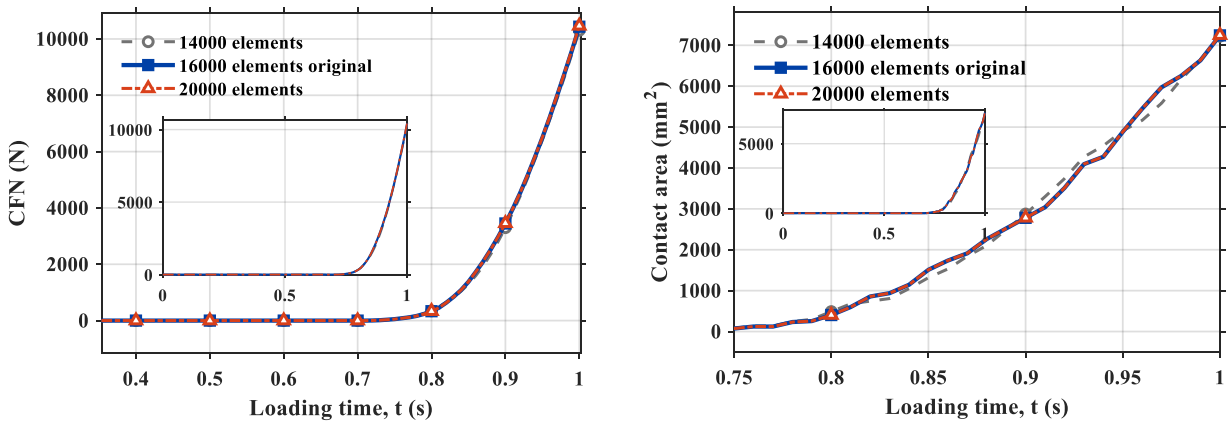


（a） (b)

Fig.15 Sensitivity Analysis of Material Parameters: (a) CFN .(b) contact area

To verify the influence of mesh density on the numerical results, three meshes containing 14,000, 16,000, and 20,000 elements were examined, with CFN and contact area under the M_3 condition selected as the evaluation metrics. As shown in Fig. 16, the three meshes exhibit essentially consistent response trends, and the terminal values obtained with 16,000 and 20,000 elements are very close. The relative differences in both CFN and contact area between these two meshes are within 5%, indicating that the mesh with 16,000 elements is sufficient to meet the

accuracy requirements of the subsequent analysis. Therefore, this mesh is adopted for all subsequent calculations.



（a） (b)

Fig. 16 Mesh-independence verification results of the sealing contact model: (a) CFN .(b) contact area

4 Results and discussion

4.1 Influence of Particle Adhesion on the von Mises Stress in the Sealing Ring

Fig. 15(a–j) compares the von Mises equivalent stress distributions of different models under the same displacement-controlled loading. In all models, the high-stress regions are mainly located at the summits and adjacent slopes of the original asperities, and their overall locations remain essentially consistent with those in the baseline model M_0. This indicates that the original rough-surface morphology determines the primary locations of stress concentration, with the stress peaks generally occurring at asperity summits and the adjacent slope-transition regions. Particle adhesion mainly alters the stress level and the extent of the high-stress regions near the asperity summits. Because the adhered particles modify the real contact area and load sharing around the asperity summits, the equivalent stress exhibits different sensitivities to particle size and coverage. Here, the term load-sharing pattern refers to the proportion of the total normal load carried by different contact locations.

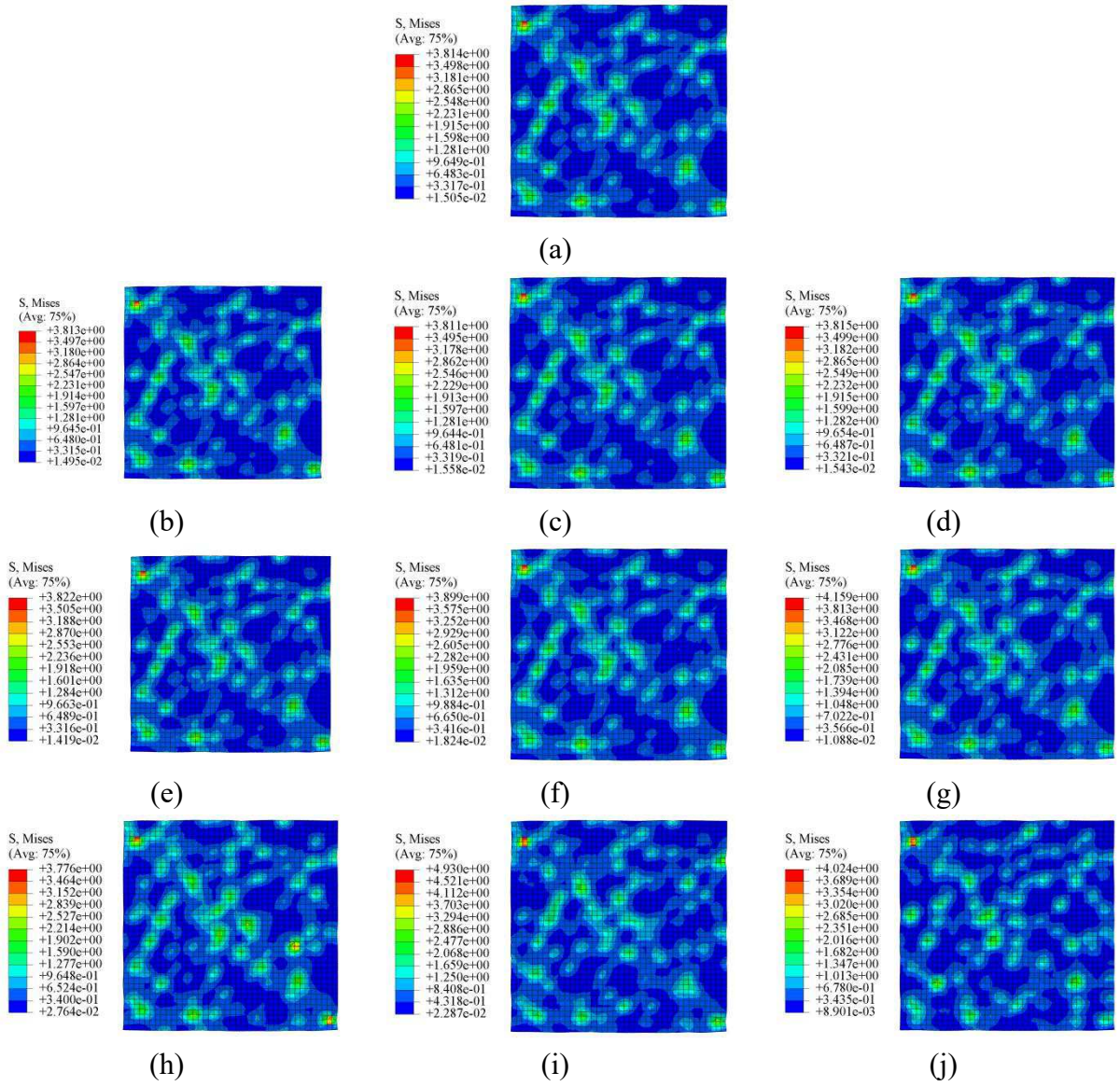
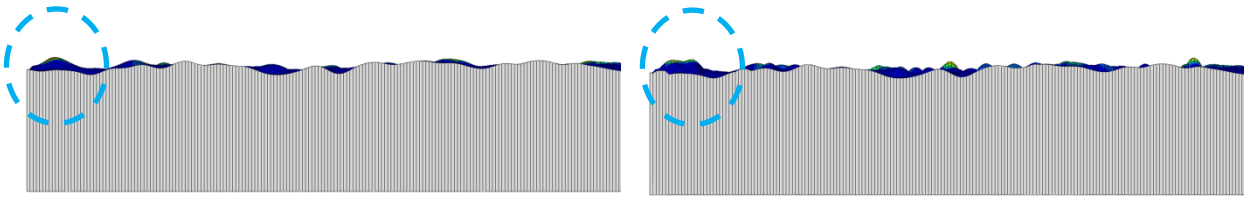


Fig.15 Mises nephogram.(a)-(j):M_0-M_9

At a fixed particle size, increasing the coverage increases both the number of adhered particles per unit area and the surface area occupied by the particles. However, the resulting effect varies with particle size. As shown by comparing Fig. 15(b), (e), and (h), when the particle size is 1.25 μm, the locations and spatial extents of the high-stress regions vary only slightly among the different coverage levels. This indicates that the local protrusions introduced by particles of this size remain limited, and that initial contact and the primary load-transfer paths are still governed by the original asperities. As the particle size increases to 2.5 and 5 μm, the effect of coverage on the equivalent-stress distribution becomes progressively more pronounced, as shown in Fig. 15(c), (f), and (i), and Fig. 15(d), (g), and (j), respectively. Higher coverage

increases the probability of particles being located at the summits and adjacent slopes of the dominant asperities, further modifying the original asperity geometry and consequently altering the contact boundaries and load-sharing locations. The influence of coverage on the equivalent stress therefore becomes more evident at larger particle sizes.

At a fixed coverage, increasing particle size produces a more pronounced effect on the equivalent stress. Comparison of Fig. 15(b–d), (e–g), and (h–j) shows that increasing particle size simultaneously increases the projected area and height scale of individual particles, thereby producing more prominent local protrusions. These changes reduce the local clearance near asperity summits and cause the seal ring to preferentially contact a limited number of higher regions. The normal load is consequently concentrated at fewer contact locations, leading to higher equivalent stresses at the asperity summits and adjacent slopes. This effect is particularly evident at coverages of 30% and 50%, indicating that the modification of local morphology and load distribution becomes more pronounced when both particle size and particle population increase.



(a) (b)_

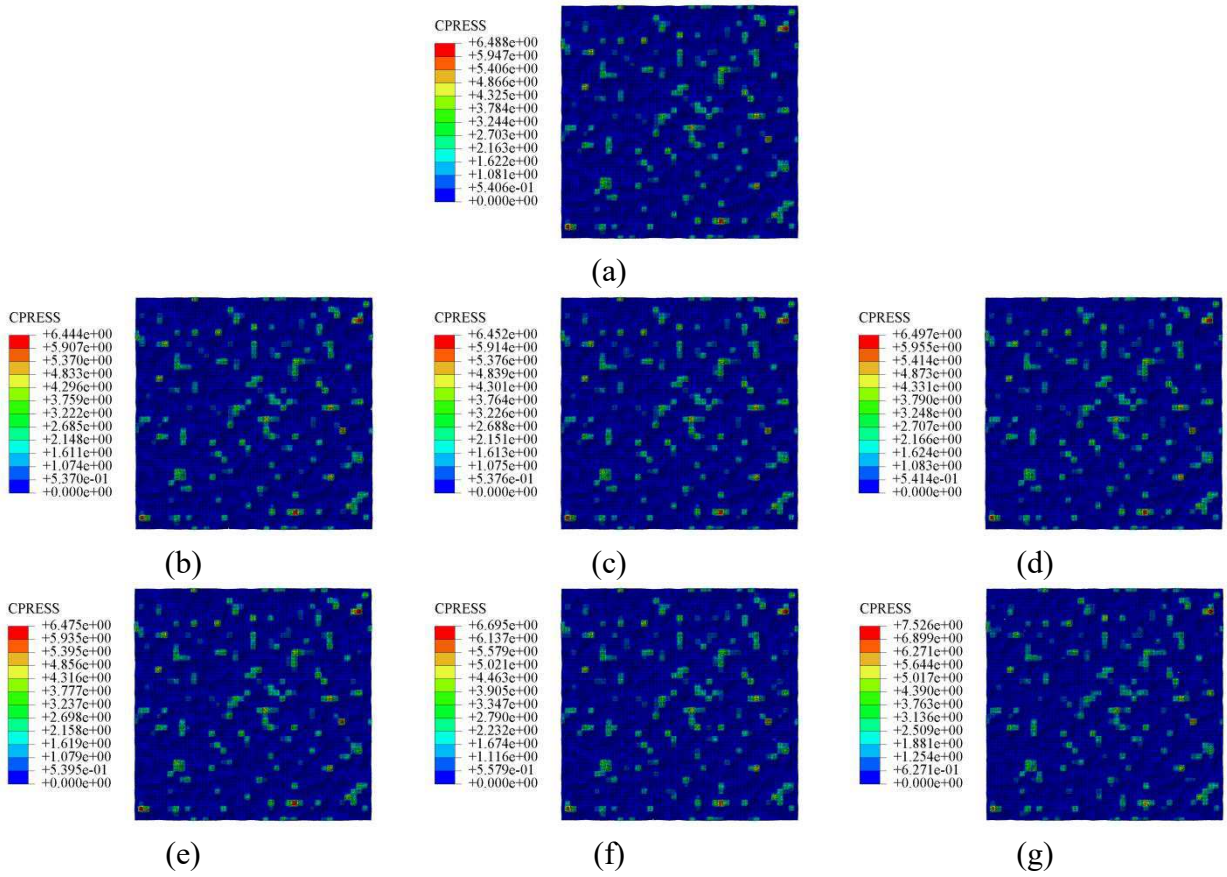
Fig.16 Comparison of true local topography between M_0 and M_8.(a)M_0.(b)M_8

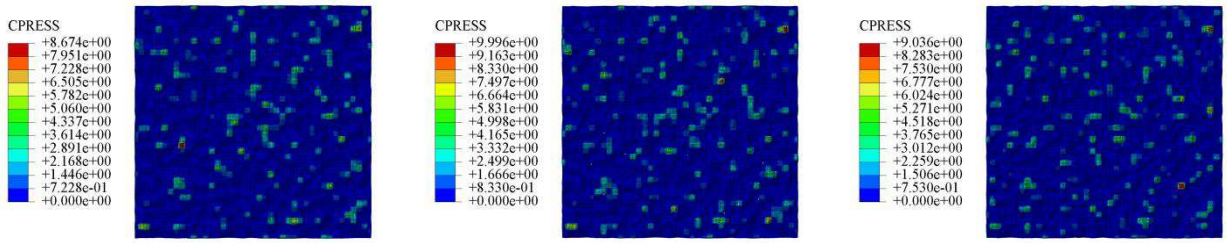
M_8 in Fig. 15(i) exhibits a substantially higher maximum equivalent stress than the other conditions. This behaviour can be attributed to the spatial coupling between particle distribution and the original asperities. Fig. 16 compares the local surface topographies of M_0 and M_8. In M_8, a larger number of particles are distributed near the dominant asperities, increasing the local protrusion height and concentrating load transfer within these regions, thereby producing a higher stress peak. Overall, the original asperities determine the locations of stress concentration,

whereas particle size, coverage, and spatial distribution jointly govern the degree of stress concentration. Among these factors, particle size exerts the more pronounced influence.

4.2Influence of Particle Adhesion on Interfacial Contact Pressure

Fig. 17(a–j) compares the spatial distributions of the interfacial contact pressure (CPRESS) under the same displacement-controlled loading. The contact pressure exhibits a discrete distribution in all models. Regions of high contact pressure are mainly located at the summits and adjacent slopes of the original asperities, and their overall locations remain essentially consistent with those in M0. This indicates that the interfacial normal load is primarily transmitted through the local real contact regions formed between the asperities and the seal ring, and that the locations of contact-pressure concentration remain controlled by the original rough-surface morphology. In contrast to the von Mises stress, which characterises the internal stress state of the seal ring, CPRESS directly represents the local normal load at the interface and is therefore more sensitive to variations in the local morphology and contact boundaries near asperity summits.





(h) (i) (j)

Fig.17 Stress nephogram.(a)-(j):M_0-M_9

At a fixed particle size, increasing the coverage increases the number of particles per unit area, although the magnitude of this effect depends on particle size. When the particle size is 1.25 μm, the locations and extents of the high-contact-pressure regions vary only slightly with coverage, as shown in Fig. 17(b), (e), and (h). This indicates that the local protrusions formed by particles of this size remain limited and that the interfacial load is still mainly carried by the original asperities. As the particle size increases to 2.5 and 5 μm, the influence of coverage on the contact-pressure distribution becomes progressively stronger, as shown in Fig. 17(c), (f), and (i), and Fig. 17(d), (g), and (j), respectively. Higher coverage increases the likelihood that particles are distributed at and around the summits of the dominant asperities, thereby modifying the local contact boundaries and load-transfer locations. The effect of coverage is therefore more pronounced for larger particles.

At a fixed coverage, increasing particle size has a more pronounced effect on contact pressure. Comparison of Fig. 17(b–d), (e–g), and (h–j) shows that the projected area and height scale of individual particles increase with particle size, resulting in greater changes in the local morphology and clearance near asperity summits. The seal ring therefore preferentially contacts a smaller number of elevated regions, concentrating the normal load within a limited real contact area and further increasing the local contact pressure. This difference becomes more evident at coverages of 30% and 50%, indicating that the influence of particle adhesion on interfacial load distribution is further amplified when particle size and coverage increase simultaneously.

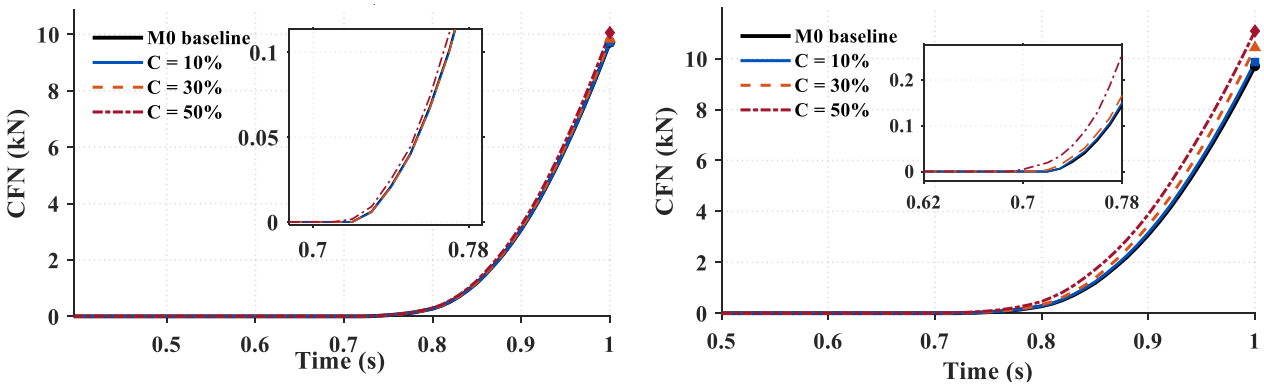
Notably, M_8 in Fig. 17(i) exhibits a substantially higher maximum contact pressure than the other conditions. The underlying mechanism is consistent with that responsible for the unusually high von Mises stress described above. A larger number of particles are distributed near the

dominant asperities, resulting in more concentrated local load transfer. Overall, the original asperities determine the primary locations of contact-pressure concentration, whereas particle size, coverage, and spatial distribution jointly govern its magnitude, with particle size exerting the stronger influence. These results also indicate that the overall interfacial contact state cannot be fully evaluated from local von Mises stress and CPRESS alone, and therefore requires further consideration of CFN, real contact area, and PAVG.

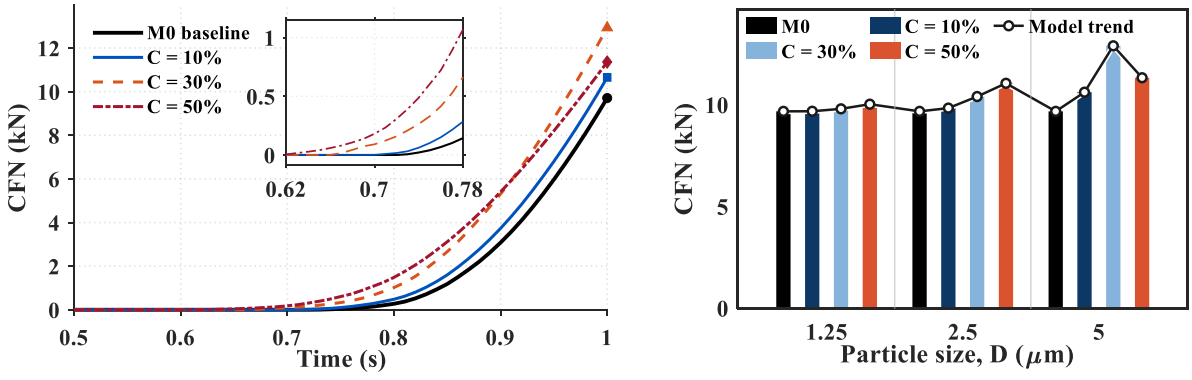
4.3 Evolution characteristics of the overall contact behaviour at the sealing interface

To compare the overall mechanical response of the sealing interface under different particle-adhesion conditions, the normal contact force (CFN), real contact area, and average contact pressure (PAVG) are analysed. These parameters characterise the normal load-bearing level, real contact region, and average pressure level of the interface, respectively. PAVG is defined as:

$$\mathrm{PAVG} = \frac{\mathrm{CFN}}{\text{Contact area}} \tag{25}$$



(a) (b)



(c) (d)

Fig. 18 Time-dependent evolution of the normal contact force under different particle adhesion conditions. The results are grouped according to particle size: (a) D=1.25μm, (b) D=2.5 μm, and (c) D=5 μm,(d)Terminal response.

Fig. 18(a–c) shows the evolution of CFN under different particle sizes and coverages. After approximately 0.6 s, CFN increases continuously with loading for all conditions. At a particle size of 1.25 μm, the curves corresponding to coverages of 10%, 30%, and 50% nearly overlap with the baseline condition, indicating a limited effect of particle adhesion on the establishment of the normal load. When the particle size increases to 2.5 μm, the curves corresponding to different coverages begin to diverge during the post-contact loading stage, with more pronounced increases at coverages of 30% and 50%. At a particle size of 5 μm, this divergence becomes more evident, and the condition with 30% coverage exhibits a faster increase in CFN. Overall, increasing particle size markedly enhances the influence of particle adhesion on normal load transfer, whereas coverage mainly affects the magnitude of CFN growth after contact is established.

Fig. 18(d) provides a direct comparison of the terminal CFN values for all models. The terminal CFN of M0 is 9.71 kN. At a particle size of 1.25 μm, the values for M1, M4, and M7 range from 9.71 to 10.06 kN and remain close to the baseline. At 2.5 μm, the range increases to 9.87–11.09 kN. At 5 μm, the terminal CFN further increases to 10.65–12.93 kN. M6 reaches the highest value of 12.93 kN, representing an increase of 33.19% relative to M0, whereas M9 decreases to 11.36 kN despite its higher coverage. These terminal results show that the differences in normal load-bearing capacity become increasingly pronounced with particle size,

while the response to coverage remains non-monotonic.

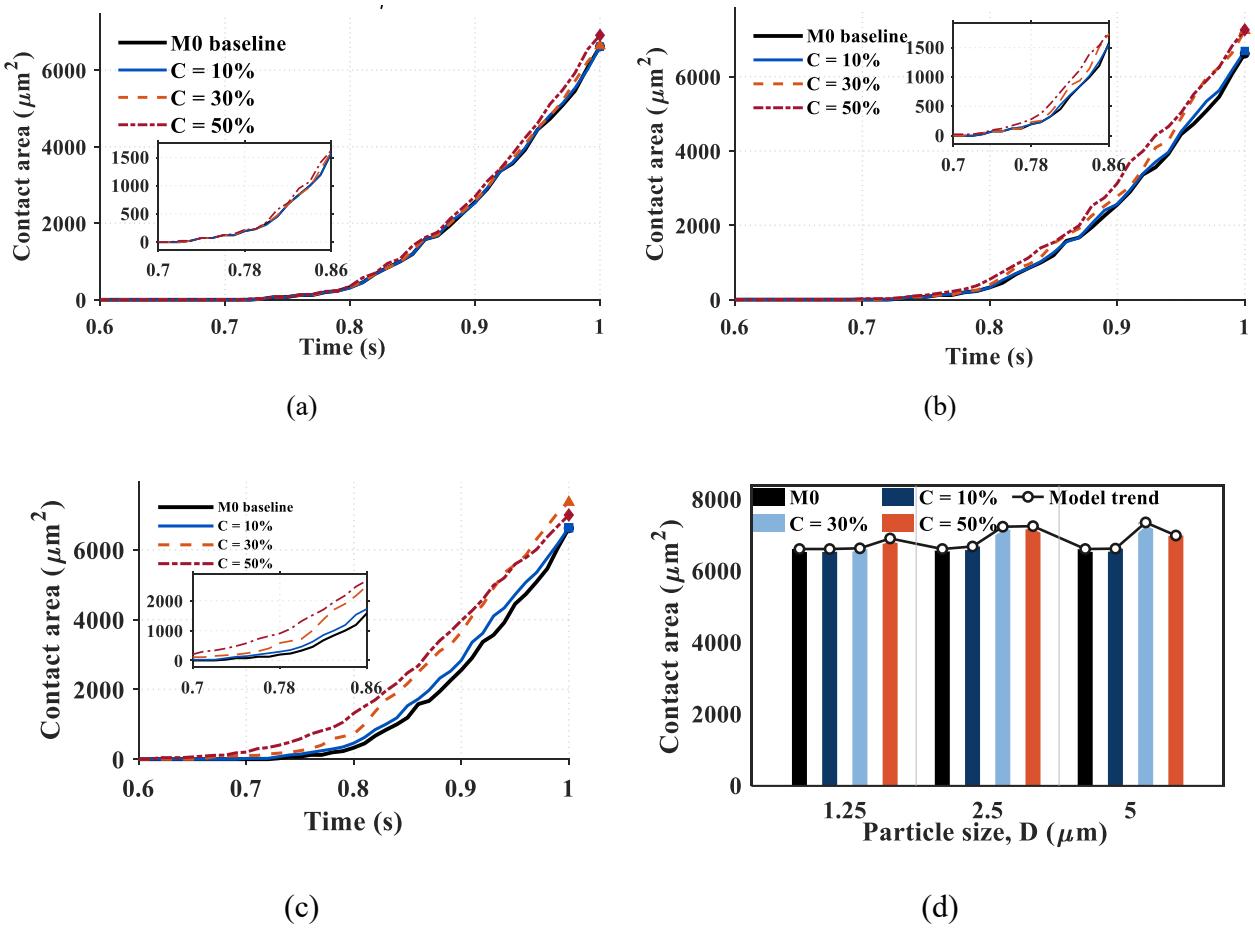


Fig. 19 Time-dependent evolution of the real contact area under different particle adhesion conditions. The results are grouped according to particle size: (a) D=1.25μm, (b) D=2.5 μm, and (c) D=5 μm,(d)Terminal response.

Fig. 19(a-c) shows the evolution of the real contact area under different particle sizes and coverages. At a particle size of 1.25 μm, the contact establishment and subsequent expansion processes at different coverages remain close to those of the baseline condition. When the particle size increases to 2.5 μm, the real contact area at coverages of 30% and 50% grows more rapidly during the middle and later stages of loading, and the corresponding curves gradually deviate from the baseline. At a particle size of 5 μm, the onset of appreciable contact advances from approximately 0.73 s for the baseline condition to approximately 0.62 – 0.69 s. Meanwhile, the differences in contact-area growth rate among the different coverages become more pronounced. These results indicate that increasing particle size promotes earlier establishment of

real contact and enhances the influence of coverage on the subsequent expansion of the contact region.

Fig. 19(d) further compares the terminal real contact areas of all models. At a particle size of 1.25 μm, the terminal values remain close to that of M_0. The relative changes in M_1 and M_4 are below 0.3%, while that of M_7 is 4.45%, indicating that particle adhesion at this size has only a limited influence on the final real contact area. When the particle size increases to 2.5 μm, the terminal contact areas of M_5 and M8 increase by 9.41% and 9.65%, respectively, demonstrating a more pronounced effect of particle adhesion on the expansion of the contact region.

At a particle size of 5 μm, M_6 exhibits the largest increase in terminal contact area, reaching 11.22%, whereas the increase for M_9 is 5.69%. Increasing the coverage from 30% to 50% therefore leads to a reduction in the terminal contact area. This indicates that, for larger particles, the real contact area does not vary monotonically with coverage and is also influenced by the spatial distribution of the particles and their relative positions with respect to the dominant asperities.

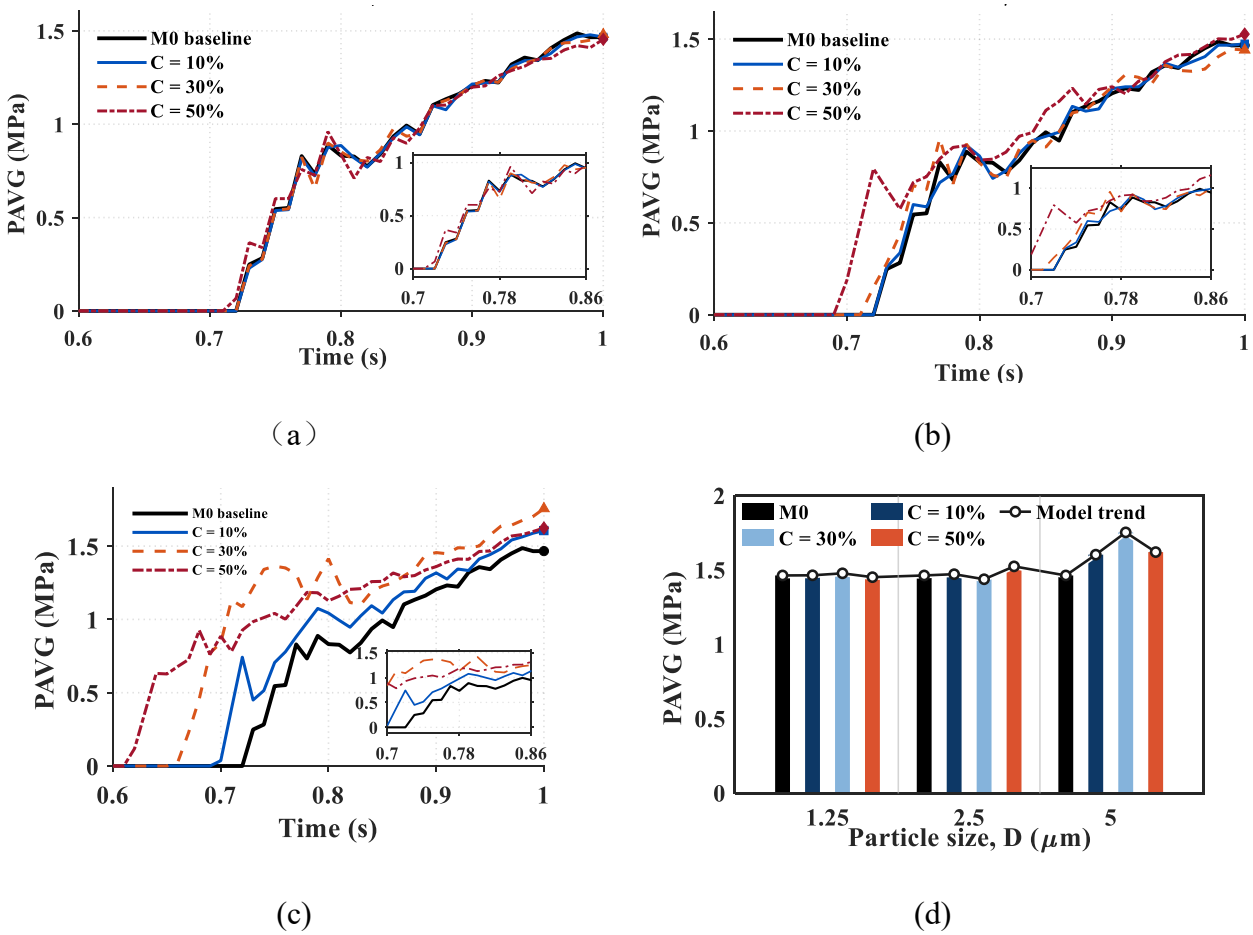


Fig. 20 Time-dependent evolution of the average contact pressure under different particle adhesion conditions.The results are grouped according to particle size: (a) D=1.25μm, (b) D=2.5 μm, and (c) D=5 μm,(d)Terminal response.

Fig. 20(a–c) shows the evolution of PAVG under different particle sizes and coverages. At a particle size of 1.25 μm, the response trajectories at different coverage levels remain generally similar, indicating that the average contact pressure is relatively insensitive to particles of this size. When the particle size increases to 2.5 μm, the curves corresponding to different coverages begin to diverge during the contact-establishment stage. At a particle size of 5 μm, this divergence becomes more pronounced. The 30% and 50% coverage conditions exhibit higher pressure responses during the middle and later stages of loading, with the increase being more pronounced at 30% coverage. These results indicate that increasing particle size amplifies the differences in interfacial load distribution among different coverage levels.

Fig. 20(d) further compares the terminal PAVG values of all models. At a particle size of 1.25 μm, the terminal PAVG values for all particle-adhered conditions differ from that of M0 by

less than 1%, indicating a limited influence of small particles on the average contact pressure. At a particle size of 2.5 μm, the terminal PAVG of M5 decreases by 1.74% relative to M0, whereas that of M8 increases by 4.16%. The opposite trends arise primarily from differences in the relative changes in CFN and real contact area.

When the particle size reaches 5 μm, the terminal PAVG values of M3, M6, and M9 increase by 9.54%, 19.76%, and 10.72%, respectively, relative to M0, indicating an overall increase in PAVG with particle size. M6 exhibits the largest increase and exceeds M9 despite the higher coverage of the latter. This confirms that PAVG does not vary monotonically with coverage, but is governed by the relative changes in CFN and real contact area.

4.4 Safety margin analysis under particle adhesion

The above results show that the variations in CFN, real contact area, and PAVG are not fully consistent across the different particle-adhesion conditions. Therefore, the overall change in the terminal contact state of the sealing interface relative to the particle-free condition cannot be adequately assessed using any single indicator. To further compare the overall deviation of the interfacial contact response under different particle parameters, a safety-margin deviation, SMdev, is introduced based on the terminal CFN, real contact area, and PAVG at t=1.0 s:

$$\begin{cases} A_i^* = \dfrac{A_{\mathrm{end},i}}{A_{\mathrm{end},0}} \\ F_i^* = \dfrac{F_{\mathrm{end},i}}{F_{\mathrm{end},0}} \\ P_i^* = \dfrac{P_{\mathrm{AVG,end},i}}{P_{\mathrm{AVG,end},0}} \\ SM_{\mathrm{dev},i} = \dfrac{|A_i^* - 1| + |F_i^* - 1| + |P_i^* - 1|}{3} \end{cases} \tag{26}$$

where A_i^*, F_i^*, and P_i^*denote the normalized terminal real contact area, normal contact force, and average contact pressure of model M_ii relative to M_0, respectively. A larger SMdev indicates a greater deviation of the terminal contact state of the sealing interface from the particle-free baseline M_0.

Tab.4 SM_{dev} of Different Models

Model	M0	M1	M2	M3	M4
SM_{dev}	0	0.0004	0.01	0.065	0.0085
Model	M_5	M_6	M_7	M_8	M_9
SM_{dev}	0.045	0.21	0.024	0.09	0.11

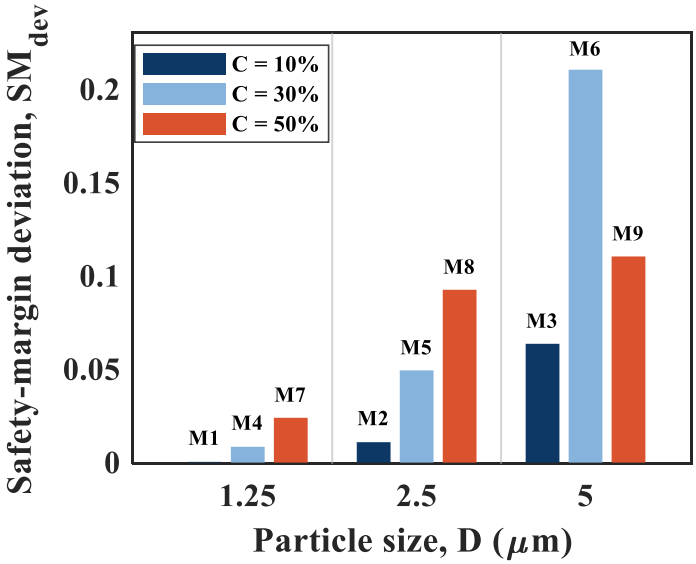


Fig.22 Comparison of SM_{dev} for different particle sizes and coverage ratios

Table. 4 lists the SMdev values under the different particle-adhesion conditions, and Fig. 22 provides a direct comparison in the form of a bar chart. At a particle size of 1.25 μm, the SMdev values of M_1, M_4, and M_7 are 0.0004, 0.0085, and 0.024, respectively, and remain at relatively low levels. This indicates that particles of this size have only a limited influence on the overall terminal contact state, even as the coverage increases.

In contrast, when the particle size increases to 2.5 μm, the SMdev values of M_2, M_5, and M_8 increase to 0.01, 0.05, and 0.09, respectively. The deviation increases progressively with coverage, indicating that the influence of coverage becomes more pronounced for particles of intermediate size.

When the particle size reaches 5 μm, the deviation in the safety margin becomes substantially more pronounced. The SMdev values of M_3, M_6, and M_9 are 0.065, 0.21, and 0.11,

respectively, all exceeding those of the smaller-particle conditions at the corresponding coverage levels. Among all models, M_6 exhibits the largest SMdev. This is mainly because the particles in this model are predominantly distributed near the dominant asperities, causing CFN, real contact area, and PAVG to deviate markedly from their corresponding values in M_0.

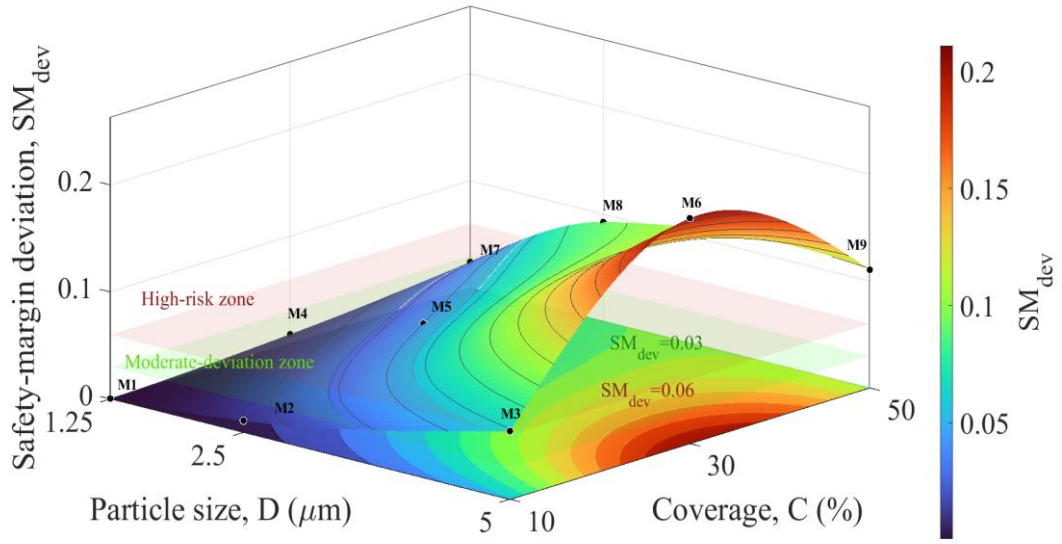


Fig.23 Safety-margin degradation and risk-zone mapping

Based on the quantitative comparison of SMdev above, Fig. 23 further maps the models onto the particle-size–coverage parameter plane to examine the distribution of the deviation under different combinations of particle parameters. The low-deviation region is mainly concentrated at D=1.25 μm. Even when the coverage increases from 10% to 50%, the terminal contact state remains relatively close to the baseline condition, confirming the limited influence of small particles on the overall contact response.

When the particle size increases to D=2.5 μm, the deviation progressively increases with coverage, indicating that particles of intermediate size begin to noticeably alter the terminal contact state at higher coverage levels. As the particle size further increases to D=5 μm, the overall deviation becomes substantially larger, with a high-deviation region developing around a coverage of 30%. In comparison, the deviation at 50% coverage is lower than that at 30%, indicating that increasing coverage does not necessarily lead to a further increase in the overall

deviation. The spatial distribution of particles relative to the dominant asperities therefore also contributes to the final contact state.

5. Conclusions

To investigate the changes in the contact state of rough sealing interfaces induced by solid-particle adhesion, an equivalent rough-surface reconstruction method incorporating particle adhesion was developed, and a three-dimensional FEM contact model was employed to analyse the effects of particle size and coverage on the interfacial contact response. Based on surface-morphology validation, local stress analysis, and evaluation of the overall contact state, the following conclusions can be drawn:

（1）The proposed equivalent rough-surface reconstruction method can reproduce the local morphological changes induced by particle adhesion while preserving the prescribed roughness level and height-distribution characteristics. Compared with the explicit particle-adhered reference surface, the equivalent particle-adhered surface shows good agreement in terms of spatial correlation and spectral distribution, demonstrating that the proposed method can effectively represent the principal morphological characteristics of a rough interface after particle adhesion.

（2）The dominant asperities of the original rough surface determine the primary locations of contact-pressure and equivalent-stress concentrations. Particle adhesion does not substantially alter the overall locations of the high-stress and high-contact-pressure regions, but modifies the local morphology and load-transfer behaviour near the asperity summits, thereby further intensifying local contact-pressure and equivalent-stress concentrations. This effect becomes more pronounced when larger particles are distributed near the dominant asperities.

（3）Particle size is the primary factor governing the overall contact state of the rough sealing interface. At a particle size of 1.25 μm, the variations in real contact area and normal contact force remain within 5%, while the average contact pressure changes only slightly. When the particle size increases to 2.5 μm, the real contact area increases by approximately 9%, and the normal contact force increases by 8%–14%. At a particle size of 5 μm, both the normal contact force and average contact pressure increase by more than 15%. These results indicate that

increasing particle size intensifies the nonuniformity of interfacial load distribution and promotes local pressure concentration. In contrast, the effect of coverage is non-monotonic and depends on the spatial distribution of particles relative to the dominant asperities.。

（4）A safety-margin evaluation method for the sealing contact state was established based on the terminal real contact area, normal contact force, and average contact pressure. Using the particle-free condition as the reference, the deviation generally remains below 0.03 at a particle size of 1.25 μm. When the particle size increases to 2.5 μm, the deviation increases with coverage and reaches 0.09, indicating an enhanced influence of coverage. At a particle size of 5 μm, the deviation remains at a relatively high level overall, with M6 reaching the maximum value of 0.21 among all conditions. These results demonstrate that larger particles are more likely to produce substantial deviations in the overall interfacial contact state, while particle spatial distribution further affects the magnitude of the deviation.

Overall, the contact state of a rough sealing interface under particle adhesion is jointly governed by the morphology of the original asperities and the local morphological modifications induced by the adhered particles. The equivalent reconstruction and contact-analysis framework developed in this study provides a basis for risk assessment and structural-parameter optimization of sealing interfaces operating in particle-laden environments. Further work should incorporate controlled particle-adhesion experiments and a larger number of stochastic surface realizations to refine the safety-margin thresholds and further establish the applicability range of the proposed model.

Credit authorship contribution statement

Haitao Zheng: has completed the writing and numerical simulation analysis. **Jialian g Wang:** has completed revision of the paper.Lubo Tang: has completed revision of the paper **Bo Li:** has drawn pictures. **Yongzheng Jang:** has supervised the simulation plan. **Buyan Wan:** has guided the design of experimental scheme.

Declaration of competing interest

The authors declare that they have no known competing financial interests or personal relationships that could have appeared to influence the work reported in this paper.

Data availability

Data will be made available upon reasonable request.

Acknowledgments

This research is supported by National Key R&D Program of China (No.2023YFC2811102, No. 2022YFC2805901), Hainan Provincial Natural Science Foundation of China (No.525MS117), Hunan Provincial Natural Science Foundation of China (No. 2025JJ50200), Hunan Provincial Department of Education Funding Project (No.25A0361), The science and technology innovation Program of Hunan Province (No. 2025RC3200), Hunan Province Science and Technology Innovation Plan Project (No. 2023ZJ1020). All authors thank the anonymous reviewers for constructive comments that helped improve this manuscript.

References

Kvenvolden, K.A., 1993. Gas hydrates—Geological perspective and global change. Reviews of Geophysics 31(2), 173–187. https://doi.org/10.1029/93RG00268.

Ruppel, C.D., Waite, W.F., 2020. Grand challenge: Timescales and processes of methane hydrate formation and breakdown, with application to geologic systems. Journal of Geophysical Research: Solid Earth 125, e2018JB016459. https://doi.org/10.1029/2018JB016459.

Wang, J., Hu, Y., Sun, Y., Wan, B., Chen, C., Yu, M., Peng, D., Tang, Y., 2024. Sealing performance analysis of pressure controller in pressure core sampling for seafloor drill. Geoenergy Science and Engineering 240, 213060. https://doi.org/10.1016/j.geoen.2024.213060.

Li, X., Zhang, X., Ma, Y., Tian, Y., Han, Z., Zhang, Y., 2024. Design and Experimental Study of an Improved Pressure Core Sampler for Marine Gas Hydrates. ACS Omega 9(13), 14977-14984. https://doi.org/10.1021/acsomega.3c09013.

Wang, J., Hu, Y., Hu, S., Yu, M., Wan, B., Tang, Y., 2025. Design and flow performance analysis of sediment core drilling tools for seafloor drill. Marine Georesources & Geotechnology 43(10), 2082-2099. https://doi.org/10.1080/1064119X.2024.2443586.

Zhou, Q., Li, S.S., Zhang, K., Wang, N., Tan, X.W., Zhou, Z.Y., Shao, T.M., Yuan, T.X., 2021. Transitions of wear characteristics for rubber/steel seal pairs during the abrasive wear process. Tribology Letters 69, 101. https://doi.org/10.1007/s11249-021-01480-4.

Zhou, Z.Y., Zhou, Q., Zhang, K., Wei, T.S.J., Di, Y.F., Wang, Y.X., Qin, K., 2024. Failure of protection against particle invasion in hard/soft dynamic seal: Modeling and observation. Engineering Failure Analysis 160, 108219. https://doi.org/10.1016/j.engfailanal.2024.108219.

Qin, K., Zhou, Q., Zhang, K., Feng, Y.L., Zhang, T., Zheng, G.J., Xia, B.R., Liu, B.L., 2019. Non-uniform abrasive

particle size effects on friction characteristics of FKM O-ring seals under three-body abrasion. Tribology International 136, 216–223. https://doi.org/10.1016/j.triboint.2019.03.051.

Chern, S.-Y., Chen, Y.-Y., Liu, W.-L., Horng, J.-H., 2022. Contact Characteristics at Interface in Three-Body Contact Conditions with Rough Surfaces and Foreign Particles. Lubricants 10(7), 164. https://doi.org/10.3390/lubricants10070164.

Chitta, S.S., Li, S., Senetakis, K., 2021. Scale and surface morphology effects on the micromechanical cont act behaviour of granular materials. Tribology International 160, 106929. https://doi.org/10.1016/j.triboint. 2021.106929.

Altuhafi, F.N., Baudet, B.A., Coop, M.R., 2024. Plastic deformation effect on contact behaviour in granular materials. Granular Matter 26, 34. https://doi.org/10.1007/s10035-024-01394-7.

Li, J., Ma, W., Hou, X., Zhang, Y., 2023. Analysis of multiscale material removal mechanism in nanoparti cle jet polishing. International Journal of Mechanical Sciences 239, 107898. https://doi.org/10.1016/j.ijm ecsci.2022.107898.

Xiao, J., et al., 2023. Coupled DEM-FEM methods for analyzing contact stress between railway ballast and subgrade considering real particle shape characteristic. Computers and Geotechnics 155, 105192. https: //doi.org/10.1016/j.compgeo.2022.105192.

Li, J.-N., Wang, J., Hu, Y.-Q., You, Z.-X., Xu, M., Wang, Y.-W., Zou, Z.-J., Kang, Q.-Y., 2022. Contact p erformance analysis of pressure controller's sealing interface in deep in-situ pressure-preserved coring s ystem. Petroleum Science 19(3), 1334–1346. https://doi.org/10.1016/j.petsci.2021.11.022.

International Organization for Standardization (ISO), 2012. ISO 25178-2:2012 Geometrical product specificat ions (GPS) — Surface texture: Areal — Part 2: Terms, definitions and surface texture parameters. ISO, Geneva.

Lehmann, P., Patzelt, S., Schöne, A., 1997. Surface roughness measurement by means of polychromatic spe ckle elongation. Applied Optics 36(10), 2188–2197. https://doi.org/10.1364/AO.36.002188.

Goryacheva, I.G., Yakovenko, A.A., 2024. The asperities density and height distribution combined effect on rough elastic bodies contact characteristics. Lobachevskii Journal of Mathematics 45(5), 2279–2292. ht tps://doi.org/10.1134/S1995080224602595.

Zhao, F.L, Ai, C.Z., Yang, DJ., et al, 2006. Study on the evaluation method andevaluation parameters of c utting surface roughness of carbon/carbon com-posite. Acta Metrol. Sin. (3), 206-211. https://doi.org/10. 3321/j.issn:1000-1158.2006.03.002 (in Chinese).

Charlton, D.J., Yang, J., Teh, K.K, 1994. A review of methods to characterise rubberelastic behaviour for u se in finite element analysis. Rubber Chem. Technol. 67 (3),481-503.https://doi.org/10.5254/1.3538686.

Wu, J.B., Li, L.,2022. Influence of ambient pressure on sealing performance of O-ring in deep-sea hydrauli c system. Ocean. Eng. 245, 110440. https://doi.org/10.1016/joceaneng.2021.110440.

Pérez-Ràfols, F., Almqvist, A., 2019. Generating randomly rough surfaces with given height probability dist ribution and power spectrum. Tribology International 131, 591–604. https://doi.org/10.1016/j.triboint.201 8.11.020

Wang, Y., Azam, A., Wilson, M.C.T., Neville, A., Morina, A., 2021. Generating fractal rough surfaces with the spectral representation method. Proceedings of the Institution of Mechanical Engineers, Part J: Jou

rnal of Engineering Tribology 235, 2640–2653. https://doi.org/10.1177/13506501211049624.

Rodriguez, N., Gontard, L., Ma, C., Xu, R., Persson, B.N.J., 2025. On how to determine surface roughness power spectra. Tribology Letters 73, 18. https://doi.org/10.1007/s11249-024-01933-6.

Seal Maker, 2021. Material data sheet U500-R95: Polyurethane U500-R95. Seal Maker Produktions- und Vertriebs GmbH.

Duncan, B.C., Crocker, L.E., Urquhart, J.M., 2000. Evaluation of hyperelastic finite element models for flexible adhesive joints. NPL Report CMMT(A)285, National Physical Laboratory.

Kut, S., Ryzińska, G., 2023. Modeling elastomer compression: Exploring ten constitutive equations. Materials 16, 4121. https://doi.org/10.3390/ma16114121.

Lee, M.K., Lee, S.H., Hur, N., Seo, Y.J., Kim, I.C., Lee, S.J., 2011. A numerical study on dynamic characteristics of counter-rotating rigid/deformable rolls in press contact. Transactions of the Korean Society of Mechanical Engineers A 35(8), 869–876. https://doi.org/10.3795/KSME-A.2011.35.8.869.